Journal of Science: Advanced Materials and Devices 9 (2024) 100776

Contents lists available at ScienceDirect

Journal of Science: Advanced Materials and Devices

journal homepage: www.elsevier.com/locate/jsamd

Research Article

Magnetic iron-based nanoparticles encapsulated in graphene/reduced graphene oxide: Synthesis, functionalization and cytotoxicity tests

Aysa Azmoudeh [a,b,*], Sencer Moral [a,c], Seyma Sari [d], Miray Türk [e], Muhammet U. Kahveci [f], Gizem Dinler Doganay [g], Duygu Ağaoğulları [a,**]

[a] Istanbul Technical University, Faculty of Chemical and Metallurgical Engineering, Department of Metallurgical and Materials Engineering, Particulate Materials Laboratories (PML), Graphene and 2D Materials Laboratory, 34469, Maslak, Istanbul, Türkiye
[b] Koç University, Department of Biomedical Science, Rumelifeneri Yolu, 34450, Sarıyer, Istanbul, Türkiye
[c] Matil Materials Testing and Innovation Lab. Inc., Graphene and Nanomaterials Laboratory, 34450, Sarıyer, Istanbul, Türkiye
[d] Istanbul Technical University, Graduate School, Chemistry Programmme, 34469, Maslak, Istanbul, Türkiye
[e] Istanbul Technical University, Graduate School, Molecular Biology-Genetics and Biotechnology Department, 34469, Maslak, Istanbul, Türkiye
[f] Istanbul Technical University, Faculty of Science and Letters, Department of Chemistry, 34469, Maslak, Istanbul, Türkiye
[g] Istanbul Technical University, Faculty of Science and Letters, Molecular Biology and Genetics Department, 34469, Maslak, Istanbul, Türkiye

ARTICLE INFO

Keywords:
Magnetic nanoparticles (MNPs)
Multilayer graphene (MLG)
Reduced graphene oxide (rGO)
Functionalization
Magnetic/thermal properties
Cytotoxicity

ABSTRACT

Nanomaterials for suitable particle sizes, shapes, surface properties, biocompatibility, magnetic properties, and chemical stability are candidates for biomedical applications. Among these nanomaterials, iron-based ones are highly interested in their morphological and magnetic properties for potential utilizations in biomedicine. However, iron-based nanoparticles lose their chemical stability in body fluids because of their oxide formations and transformations. Their use in biomedical applications, especially in imaging, may be less effective if they are oxidized and have lower magnetization values. Thus, the idea of coating them with a protective layer has recently emerged to prevent magnetic nanoparticles from degrading in human fluids and losing their magnetic properties. However, the biological effects of these coated nanoparticles on human cells are poorly understood. In this paper, the synthesis of multilayer graphene (MLG) encapsulated iron-based nanoparticles was investigated by solvothermal and chemical vapor deposition (CVD) methods followed by purification. Subsequently, their surface modification was conducted with pyrene end-functional POEGMA obtained by atom transfer radical polymerization (ATRP). Cytotoxicities of synthesized nanoparticles were evaluated in MCF7 cell lines, which is a commonly used model for breast cancer research. We also compare the results with those obtained from bare iron oxide nanoparticles (IONPs) and iron oxides that were embedded in reduced graphene oxide (rGO) or partially coated with it. We aim to evaluate the safety and efficiency of these nanoparticles and increase their chemical stability as a multifunctional nano platform for cancer diagnosis and treatment. Characterization techniques such as XRD, XPS, SEM, TEM, DTA/TG, DLS, zeta potential, BET, NMR, FTIR, and VSM were performed on the nanoparticles. Cytotoxicity assessments on MCF-7 cell lines indicated the potential of these graphene-based magnetic nanoparticles for biomedical applications, particularly drug delivery, due to their small size, soft ferromagnetic properties, high chemical stability, and cytocompatibility at concentrations below 500 μg/mL over short incubation times.

1. Introduction

These days, the biomedical field is very interested in magnetic nanoparticles (MNPs) because of their size-dependent superparamagnetic, multifunctionality, high surface area, and ease of surface modification [1–3]. Magnetic nanoparticles can be influenced by

Peer review under responsibility of Vietnam National University, Hanoi.
* Corresponding author. Istanbul Technical University, Faculty of Chemical and Metallurgical Engineering, Department of Metallurgical and Materials Engineering, Particulate Materials Laboratories (PML), Graphene and 2D Materials Laboratory, 34469, Maslak, Istanbul, Türkiye.
** Corresponding author.
E-mail addresses: aazmoudeh23@ku.edu.tr (A. Azmoudeh), bozkurtdu@itu.edu.tr (D. Ağaoğulları).

https://doi.org/10.1016/j.jsamd.2024.100776
Received 20 May 2024; Received in revised form 7 August 2024; Accepted 12 August 2024
Available online 14 September 2024
2468-2179/© 2024 Vietnam National University, Hanoi. Published by Elsevier B.V. This is an open access article under the CC BY-NC-ND license (http://creativecommons.org/licenses/by-nc-nd/4.0/).

external magnetic fields: they lose their magnetization when the field is removed [2–4]. There are several synthesis methods for obtaining MNPs. The most used methods include solvothermal [1,5,6], hydrothermal [7–9], microemulsion precipitation [10,11], laser pyrolysis [12,13], and co-precipitation [3,14–16] techniques. Among them, chemical methods are more versatile and have a low cost in producing non-agglomerated, homogeneous, and dispersed fine particles [17,18]. By coating them with appropriate materials like gold, silica, carbon-based materials, polymers, and biomolecules, magnetic nanoparticles can be safely used in biomedical applications such as biosensors [8,18–20], magnetic hyperthermia [18,21–23], magnetic resonance imaging (MRI) [24–26], drug delivery [27–29], magnetic particle imaging (MPI) [25,26,30], and tissue engineering [31,32]. This will improve the stability, dispersibility, functionality, and biocompatibility of the MNPs.

Carbon shell coatings are a subset of core-shell nanostructures that are made by covering a core material, such as metal, metal oxide, or semiconductor, with a layer of carbon [17,30,33–35]. Two-dimensional (2D) nanomaterials have large lateral dimensions and an incredibly thin structure that frequently consists of just one or a few atomic layers [12,36,37]. Because of its exceptional optical, thermal, electrical, and mechanical capabilities, graphene with honeycomb lattice structures has found extensive use in biomedical applications [34,38]. Nowadays, chemical vapor deposition (CVD) is utilized as a practical and an efficient method for coating MNPs [30,33,35]. It is easier to produce homogeneous shell structures via gas-solid phase reactions [39–43]. Additionally, low-pressure CVD inhibits the undesired gas-phase reactions and leads to the formation of pure graphitic layers [40,42].

Following the coating, the process of functionalizing graphene involves altering its surface to regulate its chemical and physical properties as well as to reduce the cohesive force between graphene sheets [33,44,45]. Enhancing graphene's processability, solubility, and compatibility with other materials is the aim of the functionalization [46]. There are copolymers such as pyrene-functionalized poly(methyl methacrylate)-*block*-polydimethylsiloxane (Py-PMMA-*b*-PDMS) synthesized via activators regenerated by an electron transfer atom transfer radical polymerization (ARGET ATRP) method and used to functionalize graphene through the π–π interaction between pyrene and the carbon sheets [44–46]. According to the study by Baihua et al. [47], Fe@C nanoparticles have lower toxicities compared to Fe_3O_4@C in human lung (A549) and skin (A431) cell lines. According to a study by Chaochao et al. [48], polymer-coated Fe_3O_4-graphene oxide nanoparticles are promising materials for both magnetic resonance and fluorescence imaging on the low toxicity observed on hepatocarcinoma cells (BEL-7402).

In this study, we synthesize ferromagnetic Fe_3O_4 with magnetization values (M_s) of 60.95 emu/g and ferromagnetic Fe_3O_4@rGO nanoparticles with M_s of 59.39 emu/g by solvothermal method. Because chemical stability affects MNPs' functionality and biocompatibility, we improve MNP chemical stability throughout the body. Chemical stability refers to MNPs' ability to withstand oxidation, dissolution, aggregation, and disintegration in biological environments like tissues, blood, or cells. MNPs may lose their magnetic characteristics, produce harmful ions, or interact unintentionally with biological components like cells, lipids, or proteins if they are not chemically stable [49]. As a result, the aim of this study is to coat multi-layered graphene on the MNPs by CVD process at 950 °C, which changes the magnetic properties of nanoparticles from ferromagnetic to soft ferromagnetic. Subsequent leaching treatments using HCl, and HF acid-containing solutions were conducted on the coated samples. In addition, the graphene-encapsulated iron--based MNPs (Fe/Fe_3C@rGO@G) were further coated with pyrene-end functional PEG-based polymer (PMA-POEGMA) synthesized via ATRP to improve dispersion properties and biocompatibility of the MNPs. Characterizations of the nanoparticles were performed using a series of techniques such as X-ray diffractometry (XRD), X-ray photoelectron spectroscopy (XPS), Raman spectroscopy, scanning and transmission electron microscopy (SEM and TEM), differential thermal analysis/thermogravimetry (DTA/TG), dynamic light scattering (DLS), zeta potential, BET analysis, nuclear magnetic resonance spectroscopy (NMR), Fourier-transform infrared spectroscopy (FTIR), and vibrating sample magnetometry (VSM). Additionally, cytotoxicity measurements of each Fe_3O_4, Fe_3O_4@rGO, and Fe-based@rGO@G@PMA-POEGMA nanoparticles were done on MCF-7 cell lines as a function of incubation times. As a result, this study claims that multilayer graphene-based

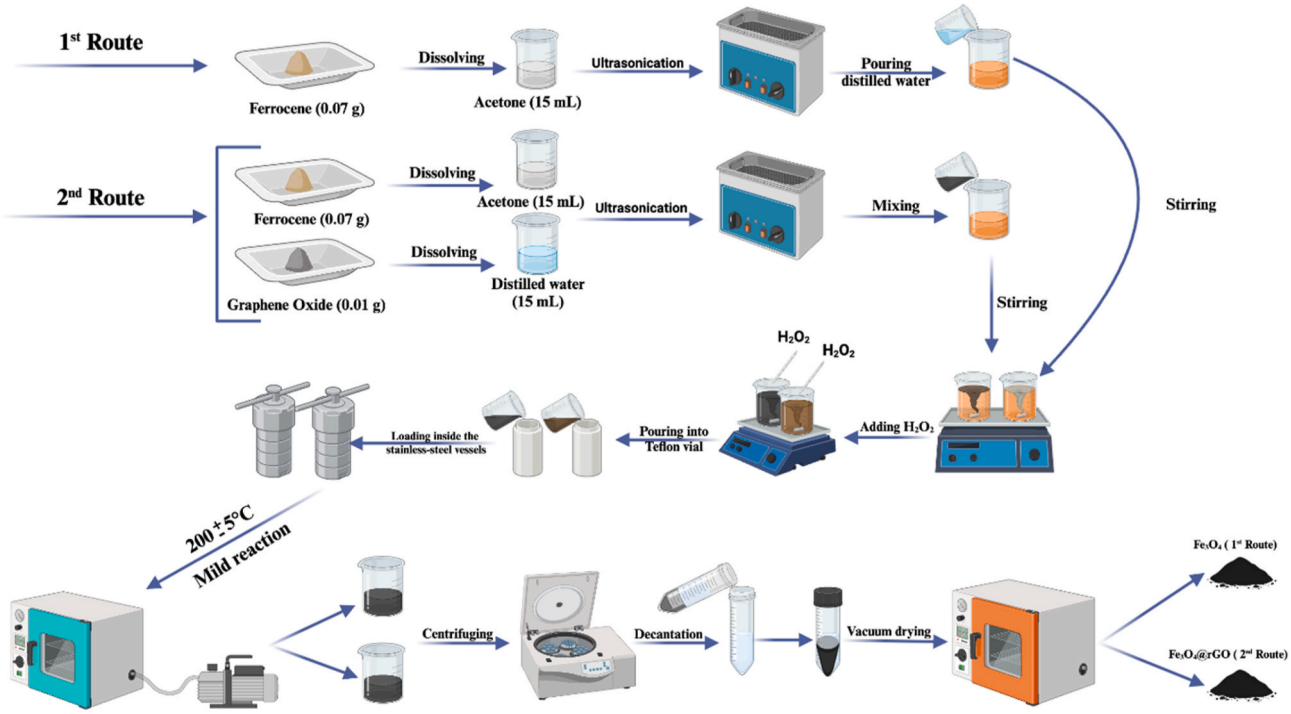


Fig. 1. Schema of all utilized steps in solvothermal synthesis of Fe_3O_4 and Fe_3O_4@rGO nanoparticles (created with biorender.com).

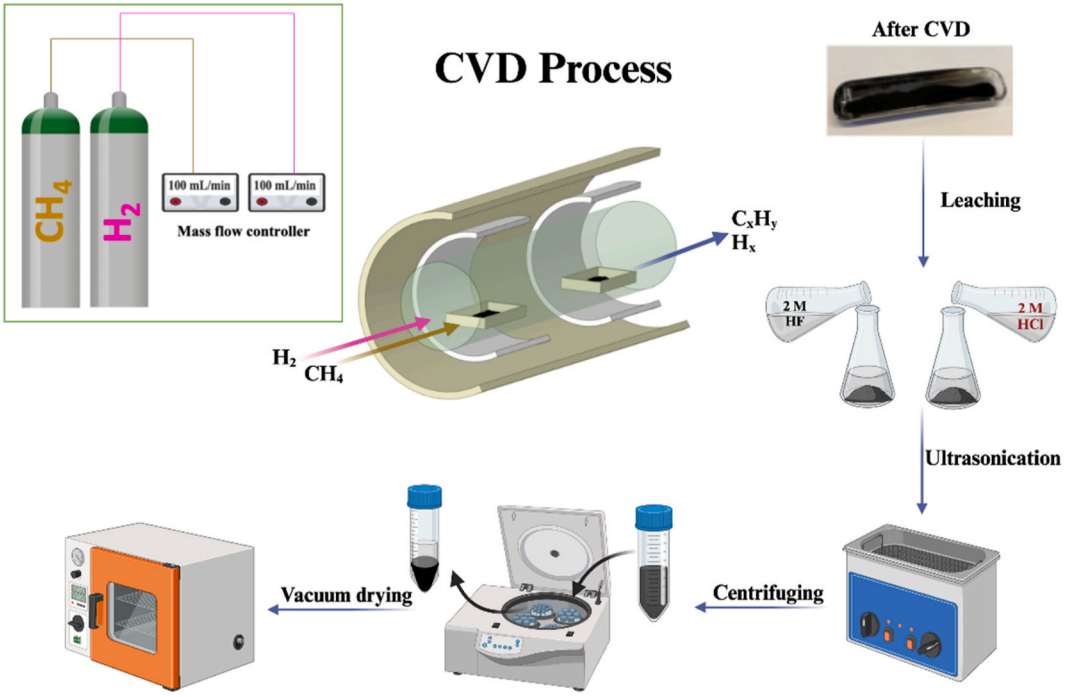


Fig. 2. Schema of all utilized steps in CVD process and purication of Fe-based@rGO@G nanoparticles (created with biorender.com).

magnetic nanoparticles can be a good candidate for biomedical applications, mostly drug delivery, due to their low particle size, soft ferromagnetic properties, high chemical stability, and cytocompatibility below 500 μg/mL at short incubation times.

2. Materials and methods

2.1. Materials

Ferrocene ($FeC_{10}H_{10}$, ISOLAB, 99% purity), graphene oxide (GO, AEROFEN), copper(I) bromide (Cu(I)Br, Sigma-Aldrich), α-Bromoisobutyryl bromide (BIBB, Sigma-Aldrich), 1-pyrenemethylamine hydrochloride (PMA, Sigma-Aldrich) were used as raw powder materials. Hydrogen peroxide (H_2O_2, ISOLAB, density: 1.13 g/cm^3), acetone (CH_3COCH_3, Tekkim, 99.5% purity), hydrofluoric acid (HF, 48% concentrated, Merck), hydrochloric acid (HCl, 37% concentrated, Merck), triethylamine (TEA, Sigma-Aldrich), *N,N,N′,N′,N″*-pentamethyldiethylenetriamine (PMDETA, Sigma-Aldrich), and poly (ethylene glycol) methyl ether methacrylate (POEGMA, average Mn 300, Sigma-Aldrich, passed through a neutral alumina column to remove the inhibitor before use), FBS (Gibco, heat-inactivated, Brazil 500 mL, 10,500,064), Penicillin-Streptomycin (Gibco, 10,000 U/mL, 15,140,122), and cell culture grade DMSO (GENAXXON, M6323.0100), and Thiazolyl Blue Tetrazolium Bromide (MTT, BIOMATIK, A3338-250 MG) were used as chemicals in the experiments.

2.2. Solvothermal synthesis of Fe_3O_4 nanoparticles

($FeC_{10}H_{10}$) powder was the starting material for synthesizing magnetic Fe_3O_4 powder. Initially, 0.07 g ($FeC_{10}H_{10}$) was mixed in the 15 mL acetone and 15 mL distilled water, and was left inside the ultrasonic stirrer for 15 min, and then H_2O_2 was added and stirred together for 30 min. After 30 min of mixing, the solution was loaded into a Teflon vial inside a stainless-steel vessel. Mild reaction conditions was provided inside the vessel during 26 h kept at 200 ± 5 °C. After reaction occurred and vessel was cooled down to room temperature, reaction products were washed using acetone. Repeated centrifugation at 6500 rpm for 10 min was used to separate the residue from the supernatant liquid. The remnant was dried in an oven at 60 °C for 18 h in the air. The residues obtained were calcined under Argon gas (Ar, Linde, 99.99% purity) flow.

2.3. Solvothermal synthesis of Fe_3O_4@rGO nanoparticles

($FeC_{10}H_{10}$) and GO powders were utilized for synthesizing magnetic Fe_3O_4@rGO powder. 0.01 g of the GO was dispersed in the 15 mL distilled water by stirring for 10 min. Then, 0.07 g ($FeC_{10}H_{10}$) was dispersed in the 15 mL acetone and ultrasonically stirred for 15 min. The solutions were mixed for 30 min by adding H_2O_2 and stirred for 30 min, then placed in a Teflon vial inside a stainless-steel vessel before autoclaving for 26 h at 200 ± 5 °C. After reaction, acetone washing, repeated centrifugation, decantation were applied and the residue was removed from the supernatant liquid. The residues were calcined using Ar atmosphere at the same condition. The representation of all experimental steps for solvothermal synthesis of Fe_3O_4 and Fe_3O_4@rGO nanoparticles are given in Fig. 1.

2.4. CVD process and purification for graphene encapsulated Fe_3O_4@rGO nanoparticles

Fe_3O_4@rGO nanoparticles were coated by multi-layered graphene; for this process, methane (CH_4, 99.99% purity, Linde), and hydrogen (H_2, 99.99% purity, Linde) were the gases utilized in the CVD process. The reaction was initially obtained with the furnace turned up and maintained at 950 °C for a predetermined time over a period of 60 min. H_2 gas entered the system at a constant flow rate of 100 mL/min. Once the furnace reached to 500 °C, 100 mL/min of CH_4 gas was introduced. The following process parameters were used in the CVD experiment as follows: reaction temperature of 950 °C, heating rate of 10 °C/min, holding time of 60 min, cooling rate of 10 °C/min, outlet pressure of 50 mbar, H_2 flow rate of 100 mL/min, and CH_4 flow rate of 100 mL/min. By using two quartz boats inside a quartz reactor (two heating zone) in the CVD system, the CH_4 dissociation and carbon deposition on the Fe_3O_4@rGO were provided, as indicated in Fig. 2. H_2 gas was continuously supplied to the reactor as CH_4 gas passed through it to hasten the decomposition of the precursor and enable the creation of *C*–C bonds.

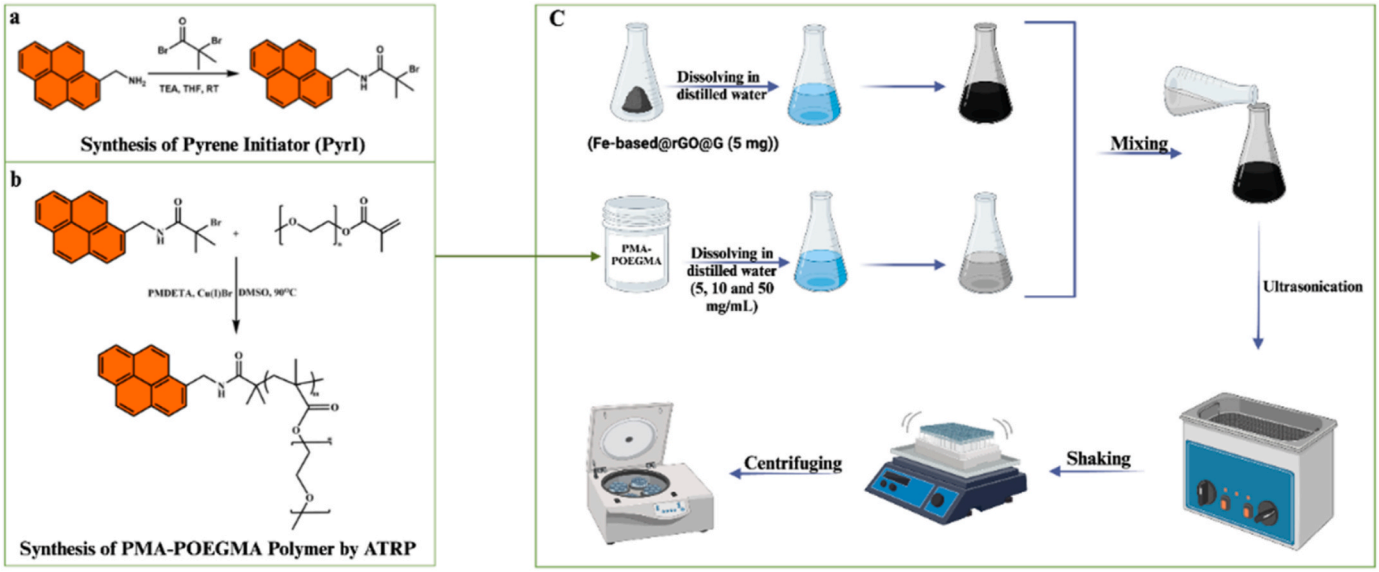


Fig. 3. Schema of all utilized steps in the (a) synthesis of Pyrene initiator (PyrI), (b) synthesis of PMA-POEGMA polymer by ATRP, (c) coating Fe-based@rGO@G nanoparticles by PMA-POEGMA (created with biorender.com).

The remaining H_x, C_xH_y, and potential effluent gases were transported to a laboratory-scale gas scrubber using a vacuum pump system. It has been proposed that employing gaseous carbon sources aids in the formation of encapsulated particles.

Magnetic Fe_3O_4@rGO nanoparticles that were encapsulated in graphene underwent two steps of purification. First, after the CVD procedure, the non-encapsulated content of the produced powders was removed utilizing a hydrofluoric acid (HF) solution. Graphene encapsulated nanoparticles were considered insoluble in the HF solution at that time. Due to this, a 2 M HF solution (48% concentrated, Merck) was used, with a solid-to-liquid concentration of 8 mg/mL to the post-CVD powders. After being leached with HF solution for 1 h and swirled with an ultrasonic device, the acidic solution material was left at room temperature. To get powders free of contaminants, the subsequent stages of centrifugation at 4500 rpm, 10 min, decantation, and filtration were carried out three times. Subsequently, non-encapsulated nanoparticles were removed using a 37% concentrated hydrochloric acid (2 M HCl) solution. The HCl leaching procedure was crucial for determining the encapsulated nanoparticles' chemical stability. HCl leaching process was conducted for 1 h before being left at room temperature overnight. The supernatant liquid was decanted, the remaining solids were centrifuged to precipitate the solids, and the solids were then washed four times with distilled water. Lastly, Fe-based@rGO@G nanoparticles were produced by drying the resulting powders in a furnace overnight at 100 °C in the air. The schema of all utilized steps in the CVD process and purication of Fe-based@rGO@G nanoparticles is shown in Fig. 2.

2.5. Functionalization of nanoparticles

2.5.1. Synthesis of PMA-POEGMA polymer

Metal nanoparticles and graphene-based materials can not be dispersed in aqueous media, and mostly, they are coated with hydrophilic materials such as proteins and poly(ethylene glycol) (PEG) to enhance their colloidal stability in physiological environments. In this regard, pyrene-end functional poly(oligo(ethylene glycol)methacrylate) (PMA-POEGMA) was selected as the hydrophobic coating material for the NPs. For the preparation of the designed polymer, a pyrene functional ATRP initiator (PyrI) was synthesized. Briefly, 1-pyrenemethylamine hydrochloride (PMA) (116 mg, 4.33×10^{-4} mol) was dissolved in 10 mL THF in a round bottom flask, which was repeatedly degassed and filled back up with N_2 gas three times. After the addition of TEA (362 μL, 2.6×10^{-3} mol), BIBB (267.8 μL, 2.17×10^{-3} mol) was slowly added into the flask using a syringe at 0 °C, and the temperature was raised to room temperature gradually. The reaction mixture was stirred for 24 h. The mixture was filtered, and the crude solid product was purified by recrystallizing from CH_2Cl_2/ethanol. The product was filtered, washed with excess cold ethanol, and dried under vacuum (Yield: 86%).

In the next step, PMA-POEGMA polymer was synthesized by ATRP. Monomer (OEGMA, 2.00 g, 6.67×10^{-4} mol, 30 eq.), ligand (PMDETA, 77 mg, 4.44×10^{-4} mol, 2 eq.), catalyst (CuBr, 38 mg, 2.67×10^{-4} mol, 1.2 eq.), the initiator (PyrI, 84.5 mg 2.22×10^{-4} mol, 1 eq.) and dimethylsulfoxide (DMSO) were added, consecutively, into a Schlenk tube equipped with a magnetic stirring bar. The polymerization solution was degassed by three freeze-pump-thaw cycles and then placed in a thermostated oil bath (90 °C) for 24 h. After the polymerization, the polymer was dialyzed against H_2O for 48 h in a dialysis membrane (MWCO 1 kDa) to remove excess Cu ions and further purification. The polymer was dried via lyophilization (Yield: 75%, $M_{n,GPC} = 21{,}500$, $M_w/M_n = 2.2$) [50].

2.5.2. Coating of PMA-POEGMA polymer

The PMA-POEGMA was then utilized for coating Fe-based@rGO@G nanoparticles. Briefly, 5 mg of sample dispersed in 5 mL of distilled water was mixed with 5 mL of an aqueous solution of PMA-POEGMA containing different amounts (5, 10, and 50 mg/mL). Afterward, the mixtures were further dispersed in an ultrasonic bath for 10 min, and kept in a shaker for 24 h at ambient temperature. A representation for the polymer coating of the Fe-based@rGO@G nanoparticles is given together with polymer synthesis steps in Fig. 3.

2.6. Cell culture and cytotoxicity test of MNPs in the MCF-7 cell lines

MCF-7 cells were cultured in DMEM high-glucose (Thermo Fisher, 41,966,029) supplemented with 10% FBS (Gibco 10,500,064) and 1% Penicillin/streptomycin (Thermo Fisher, 10,000 U/mL, 15,140,122) in a humid incubator at 37 °C with 5% CO_2. Upon reaching 80–90% confluency, measured by the cell counting device (EVE, NanoeEntek), cells were harvested by trypsinization, and 3×10^3 cells were seeded to each well of the 96-well plates in 100 μL media and incubated in the incubator for growth. Same day, stock solutions of the nanoparticles were

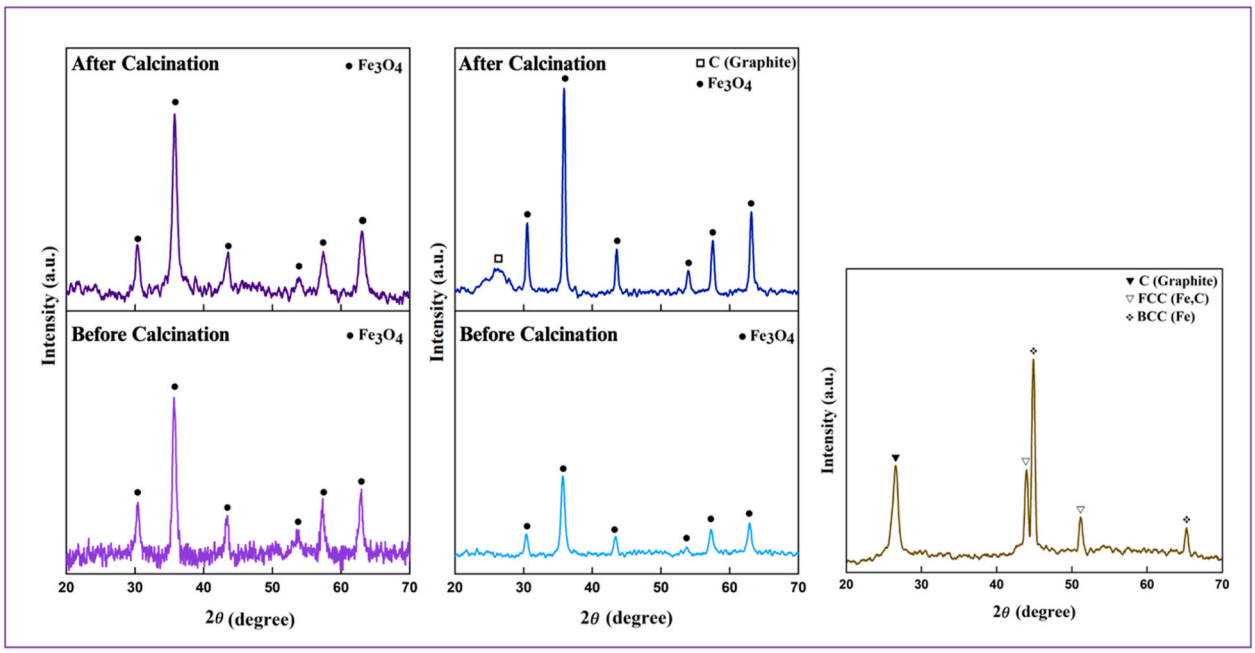


Fig. 4. (a) XRD patterns before and after the calcination process of the solvothermally synthesized Fe_3O_4, (b) before and after the calcination process of the solvothermally synthesized Fe_3O_4@rGO, (c) after CVD process of Fe_3O_4@rGO MNPs.

prepared in cell culture grade DMSO (Genaxxon, M6323.0100) at 25 mg/mL concentration, and mixed gently overnight. Stock solutions were diluted to certain concentrations via DMSO by serial dilution. Cells were treated with a specific final concentration of nanoparticles ranging from 5×10^{-5} μg/mL to 5×10^{2} μg/ml by serial dilution. Since nanoparticles were diluted in DMSO, it was used as the negative control for treatment, and DMSO concentration was kept at 2% in each condition, which was determined as the maximum limit. Each condition was prepared as at least three replicates. Additionally, no-cell control for each dosage was also added to prevent possible precipitation events that may affect spectroscopic measurement. The average absorbance value of each no-cell treatment condition was subtracted from the related cell-treatment condition. Relative cell viability was then calculated compared to DMSO control. Cytotoxicity was measured upon 6 h, 24 h, 30 h, 48 h or 72 h incubation. MTT (BIOMATIK, A3338-250 MG) reagent was added at the last 3 h of each incubation. At the end of incubation, media was removed, and formazan crystals were dissolved in 100 μL DMSO. Absorbance measurement was performed at 570 nm with background correction at 630 nm by microplate spectrophotometer (Benchmark Plus Microplate Reader, Biorad). Graphs were prepared by GraphPad Prism 8.01.

2.7. Characterization investigations

Phase analyses of the powders were conducted using a Bruker Advanced Series XRD equipped with CuK_α X-ray source (operating conditions: 35 kV, 40 mA, 1.54060 Å, 2°/min scan speed, and 20–70° scan range with 0.02° increments). Fe_3O_4@rGO and graphene-encapsulated MNPs were characterized by Raman spectroscopy (Renishaw InviaRaman Microscope) using an excitation laser source of 532 nm at room temperature. X-ray photoelectron spectroscopy (XPS) technique was used on a Thermo K-Alpha photoelectron spectrometer for analyses of the Fe, C, and O elements for Fe_3O_4@rGO and graphene-encapsulated iron-based magnetic nanoparticles. Differential thermal analysis/thermogravimetric analysis apparatus (DTA/TG, Netzsch STA 449 F^3) was used to investigate the thermal properties of the MNPs before and after the CVD process. The powders (~10 mg) were placed into alumina crucibles, and heated in air up to 700 °C with 10 °C/min increments. Lake Shore 7407 vibrating sample magnetometer (VSM, Kel-F non-magnetic sample kit) was used to determine the magnetic behavior of all nanoparticles, and measurements were conducted at room temperature with a maximum applied field of 10,000 Oe. For the morphology of MNPs, a scanning electron microscope (SEM, operated at 10–15 kV), combined with an energy-dispersive spectroscope (EDS) on all nanoparticles' morphology using a Thermoscientific Quattro S equipment, and the powders were dispersed in ethanol to prevent powder agglomeration before being individually put onto the aluminum foil and dried. The detailed morphological characterization of rGO/graphene encapsulated magnetic nanoparticles was conducted using The HT7800, a 120 kV scanning transmission electron microscope S (TEM) equipped with an energy dispersive X-ray (EDX) detector. Zeta potential and particle size distribution (PSD, Malvern Mastersizer 2000) were performed for nanoparticles before and after the CVD process at room temperature. BET surface area and porosimetry analysis were conducted using a Micromeritics ASAP 2020 HD for the powders obtained before and after the CVD process. An Agilent NMR System VNMRS 500 Spectrometer was used for the ^1H NMR analysis at room temperature in $CDCl_3$ solvents with $Si(CH_3)_4$ as an internal standard. Fourier transform infrared (FT-IR) measurements were performed on a PerkinElmer FT-IR spectrum one spectrometer instrument at 4000-400 cm^{-1} scanning range with ATR accessory. Absorbance measurement for cell viability was performed at 570 nm by microplate spectrophotometer (BIO-RAD Benchmark Plus) after and before the CVD process of MNPs.

3. Results and discussion

3.1. XRD, Raman, and XPS characterization

XRD patterns of the solvothermally synthesized Fe_3O_4 and Fe_3O_4@rGO MNPs before and after the calcination process, and Fe_3O_4@rGO MNPs after CVD process are illustrated in Fig. 4a–c. The diffraction peaks and their positions of the patterns belonging to the Fe_3O_4 and Fe_3O_4@rGO were consistent with the standard XRD data for magnetite syn(Fe_3O_4)-cubic (ICSD 01-087-2334), and these structures illustrated a cubic crystal system [51,52]. The planes for the diffraction peaks at 2θ of 30.11°, 35.47°, 43.14°, 53.43°, 57.05° and 62.61° were

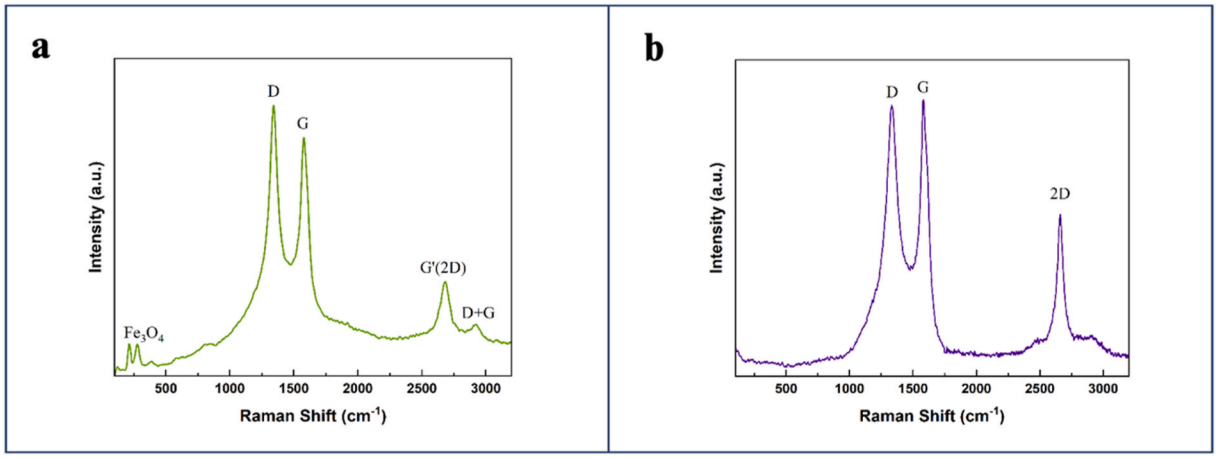


Fig. 5. Raman spectra of the (a) Fe_3O_4@rGO, and (b) Fe-based@rGO@G MNPs.

indexed as (220), (311), (400), (422), (511) and (440), respectively. The main peak of Fe_3O_4 occurred at 35.47° as shown in both graphs of Fe_3O_4 and Fe_3O_4@rGO [51–54]. Crystallinity and intensity of nanoparticles were increased after calcination for both samples, as observed from the sharp peaks in the XRD graphs (Fig. 4a and b). In one study, Zorka et al. [54]. showed that an increase in calcination temperature leads to an increase in the crystallite size, so during longer calcination time at lower temperatures, smaller crystallites were generated, while shorter calcination, lasting 4 h at 550 °C, produced slightly better crystallites. As a result, the duration of our calcination process, as shown in the patterns, is sufficient. It should be pointed out that the carbon peak is visible at 27° in Fig. 4b, after the calcination process of Fe_3O_4@rGO. Besides, the XRD pattern after the CVD process for Fe_3O_4@rGO sample is shown in Fig. 4c: the presence of the carbon peak is highly demonstrated at 27°. The furnace temperature was raised to 950 °C for 60 min with a flow rate of 100 mL/min of CH_4 gas and 100 mL/min of H_2. The powders at the boats were both covered with a layer of carbon. These formations are linked to the high rate of CH_4 flow and high temperature-induced carbon deposition [55,56]. The patterns of the powders reveal that they contain a significant quantity of C phase (graphite, ICDD card number: 01-075-2078), as shown in Fig. 4c. Due to a high temperature (950 °C) in the tube furnace, the extra reduction has occurred, and syn(Fe_3O_4)-cubic phase converted into BCC Fe (ICDD card number: 00-01-1252) phase, and FCC (Fe, C) (ICDD card number: 00-052-0513) phase. These phases (BCC Fe and FCC (Fe, C)) observed from the XRD patterns are in good agreement with the previous studies related with the decomposition of CH_4/H_2 gas mixtures [53,55–57]. After CVD process, the nanoparticles are converted to Fe-based@rGO@G (containing BCC Fe and FCC (Fe,C) phases) form from initial Fe_3O_4@rGO structure.

Raman spectroscopy is crucial in characterizing of carbon-containing materials, particularly in examining their crystal structure or crystallinity [58–61]. Fig. 5a illustrates the solvothermally synthesized Fe_3O_4@rGO nanoparticles. Fe_3O_4 bonds are observed at the Raman shifts of 208.55, 273.30, and 388.20 cm^{-1} [58,59]. The D vibration band, resulting from the mode of j-point photons of A_{1g} symmetry, is present at 1343.98 cm^{-1} for Fe_3O_4@rGO. Additionally, the G vibration band, arising from the first-order scattering of E_{2g} phonons by sp^2 carbon [58], appears at 1581.87 cm^{-1} for Fe_3O_4@rGO. The Raman spectra in Fig. 5 shows the D and G bands symbolizing disorder and tangential bands, respectively. Defects in graphene activate the D band, and the 2D band is highly sensitive to the stacking of graphene layers [58,59,62]. The presence of oxygen-containing functional groups is indicated by the shifted location of the 2D band at 2678.20 cm^{-1} in Fig. 5a for Fe_3O_4@rGO. The reduction of graphene oxide to the rGO results in fewer

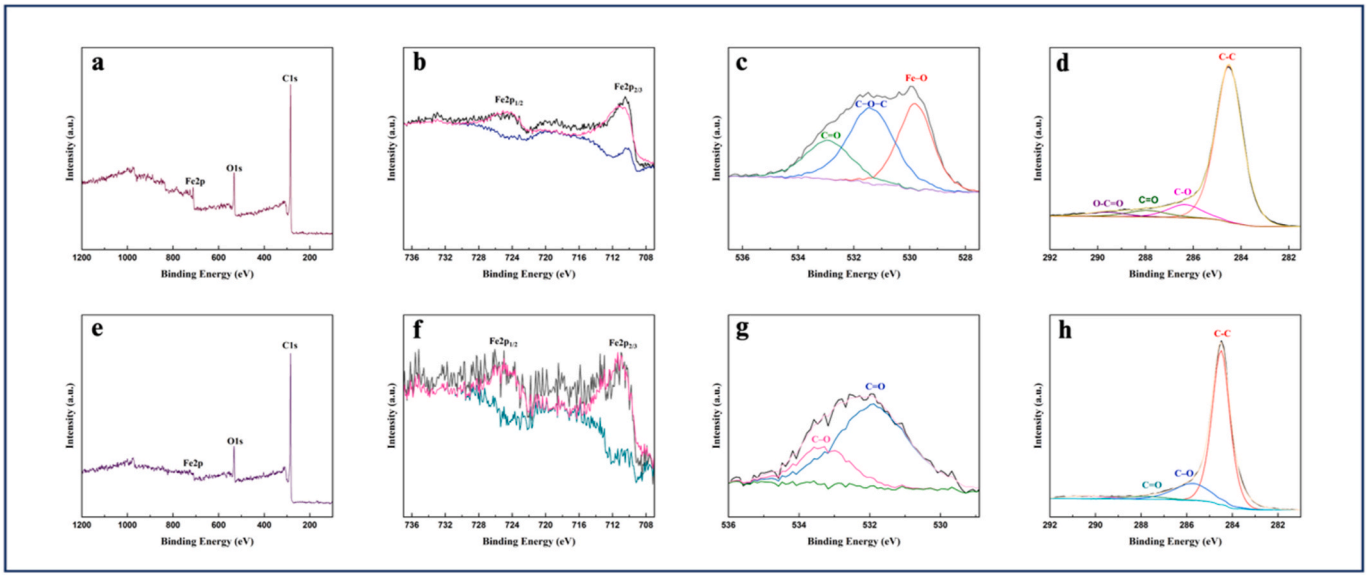


Fig. 6. XPS survey spectra of (a) Fe_3O_4@rGO MNPs and their (b, c, d) Fe2p, O1s and C1s regions, respectively, and XPS survey spectra of (e) Fe-based@rGO@G MNPs, and their (f, g, h) Fe2p, O1s and C1s regions, respectively.

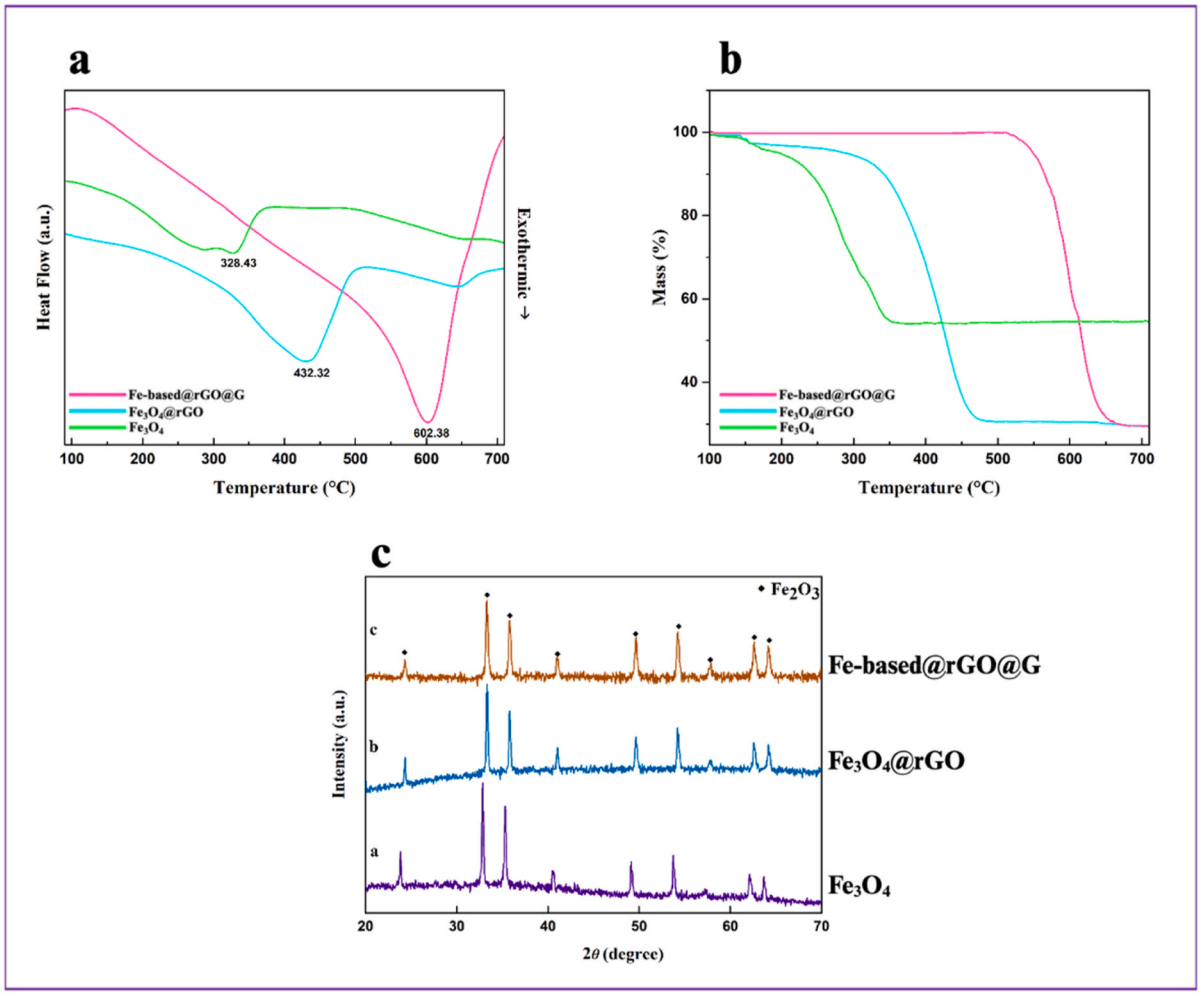


Fig. 7. (a) DTA curves, (b) TG curves, and (c) XRD patterns of the DTA residues of the Fe_3O_4, Fe_3O_4@rGO, and Fe-based@rGO@G MNPs.

residual oxygen-containing functional groups, causing rGO to stack [63–65]. Sharp D and G bands, along with a G′(2D)-band, illustrate the recovery of sp^2 C–C bonds in Fe_3O_4@rGO. The D + G bond, shown at 2930.34 cm^{-1} in Fig. 5a, confirms the presence of sp^2 carbon atoms in the reduced graphene oxide sheets [63,65,66]. Fe_3O_4 nanoparticles are attached to rGO sheets through solvothermal synthesis, reducing oxygen-containing functional groups and probably enhancing electrical conductivity [62]. The intensity ratio between the D band and the G band (I_D/I_G) is a key metric for estimating the graphitization degree of carbon materials. For Fe_3O_4@rGO, the I_D/I_G ratio is 0.83 due to the restoration of sp^2 carbon and a decrease in the average sizes of sp^2 domains upon reduction [66–68]. The higher intensity in the D band also suggests the presence of more isolated graphene domains in Fe_3O_4@rGO. Furthermore, the I_{D+G}/I_G ratio, reflecting the degree of disorder and defect in the rGO sheets, is determined to be 1.85. After coating with graphene by CVD methods, the Raman spectroscopy in Fig. 5b reveals shifts in the D, G, and 2D bands at 1330.12, 1584.41, and 2663.53 cm^{-1}, respectively. The increased I_D/I_G ratio of 0.98 after coating suggests a conversion from amorphous carbon to nanocrystalline graphite, aligning with the three-stage theory [63,66–68]. Also, the intensity of the D peak in Fe_3O_4@rGO decreases from 5257 to 4338 cm^{-1} for Fe-based@rGO@G sample, and the intensity of the G peak decreases from 4736 to 4417 cm^{-1} and for the 2D peak increases from 2481 to 2836 cm^{-1}, respectively.

XPS survey spectra of the Fe_3O_4@rGO and Fe-based@rGO@G MNPs and their Fe2p, O1s and C1s regions are illustrated in Fig. 6a–h. XPS measurements provided additional confirmation of the samples' surface chemical composition. Fig. 6 proves the scan spectra of the Fe_3O_4@rGO and Fe-based@rGO@G, where peaks of Fe2p, O1s, and C1s verify the presence of Fe, O, and C in the synthesized materials [69]. A discernible drop in the strength of Fe2p and O1s peaks is observed in the survey scan spectra of Fe-based@rGO@G (Fig. 6f) as compared those of Fe_3O_4@rGO sample (Fig. 6b). This decrease is attributed to the reduced amount of Fe_3O_4 and formation of Fe phase by the help of high-temperature operations during CVD. Furthermore, the Fe-based@rGO@G nanoparticles exhibit higher C1s peak intensity (Fig. 6h), indicating the incorporation of graphene. The Fe2p XPS spectrum, shown in Fig. 6b and f, has large peaks at roughly 710.48, 710.88, and 724.38, 725.48 eV that are indicative of the $Fe2p_{3/2}$ and $Fe2p_{1/2}$ states, revealing the existence of Fe_3O_4 or Fe in Fe_3O_4@rGO and Fe-based@rGO@G, respectively [39,70,71]. The O1s XPS spectra of Fe_3O_4@rGO and Fe-based@rGO@G, displayed in Fig. 6c and g, demonstrate the integration of rGO into the matrix. The Fe_3O_4@rGO has multiple distinct peaks at approximately 529.87, 531.38, and 532.98 eV, which correspond to Fe–O, *C*–*O*–C, C═O, and possibly other oxygen-containing groups. The C═O and *C*–O functions are attributed to two peaks that are present in Fe-based@rGO@G nanoparticles, which are centered at roughly 531.88 and 533.38 eV, respectively [69,71–73]. Binding energies of roughly 284.48 eV for *C*–C, 286.35 eV for *C*–O, 287.88 eV for C═O, and 289.28 eV for *O*–C═O C1s peak for Fe_3O_4@rGO (Fig. 6d), and those for Fe-based@rGO@G nanoparticles (Figs. 6h), 284.48 eV for *C*–C, 285.78 eV for *C*–O, 278.48 eV for C═O, indicate the presence of rGO and

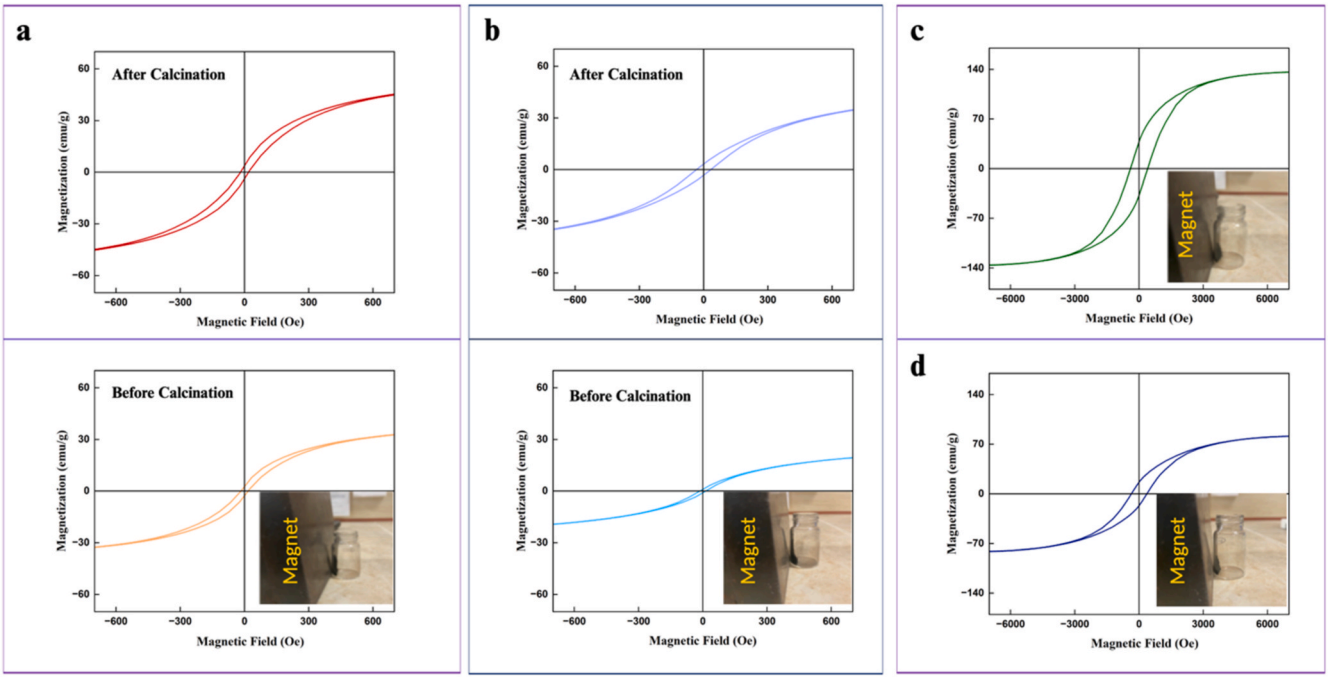


Fig. 8. Magnetic hysteresis loops of the (a) Fe_3O_4 MNPs before and after the calcination process, (b) Fe_3O_4@rGO MNPs before and after the calcination process, (c) Fe-based@rGO@G MNPs, and (d) Fe-based@rGO@G@PMA-POEGMA MNPs.

graphene in the structures [70,74].

3.2. DTA/TG analyses

The thermal behaviors of the three different nanoparticles, Fe_3O_4, Fe_3O_4@rGO, and Fe-based@rGO@G, up to 710 °C under airflow were investigated, and Fig. 7a and b, show the samples' DTA and TG curves, respectively. For the Fe_3O_4, Fe_3O_4@rGO, and Fe-based@rGO@G samples, exothermic reactions were found at 328.43 °C, 432.32 °C, and 602.38 °C, respectively. These peaks show the deterioration ranges of the nanoparticles by the effect of temperature [69]. The increased carbon content in the Fe-based@rGO@G powders provides durability for the iron-based core, and the exothermic peaking point shifts to a higher temperature (Fig. 7a). The mass reduction of the samples is evident in Fig. 7b due to the exothermic reaction that led to weight loss owing to the conversion of carbon-to-carbon dioxide [39]. In other words, the weight losses are related to volatiles evaporating [70]. During heating, the powdered forms of Fe_3O_4, Fe_3O_4@rGO, and Fe-based@rGO@G lost 45, 69, and 70 wt% of their total contents. The presence of graphene (carbon) encapsulation contributed to the greater carbon content of Fe-based@rGO@G powders, as demonstrated by the XRD and Raman studies. Thus, when the Fe-based@rGO@G powders were heated, the greatest weight reduction occurred because carbon was removed compared to the Fe_3O_4 and Fe_3O_4@rGO NPs. The larger carbon content of the Fe_3O_4@rGO powders (69 wt%) than the Fe_3O_4 powders (45 wt%) can also be attributed to the presence of rGO, which is partially coated and embedded in NPs. Since uncoated Fe_3O_4 nanoparticles were eliminated during purification, this demonstrated that all Fe-based nanoparticles were covered in multi-layered graphene shells. Also, XRD analyses of the Fe_3O_4, Fe_3O_4@rGO, and Fe-based@rGO@G after DTA and TG were illustrated in Fig. 7c. All of the samples converted to Fe_2O_3 phase (ICSD 98-005-3824), and the magnetic NPs change to hematite iron oxides by the effect of temperature. So, the encapsulation of the Fe-based cores delayed the deterioration of the overall nanoparticles.

3.3. VSM measurements

The magnetization of NPs can be changed by different factors, such as the particle size, volume, and presence of adsorbed oxygen [75]. The magnetic properties of Fe_3O_4 and Fe_3O_4@rGO nanoparticles before and after the calcination were obtained and presented in Fig. 8a. The saturation magnetization values (M_s) before and after the calcination are 41.90 emu/g and 60.95 emu/g for Fe_3O_4, whereas they are 33.10 emu/g and 59.39 emu/g for Fe_3O_4@rGO, respectively. Also, the coercivity values (H_c) are 13.16 Oe and 13.58 Oe for Fe_3O_4 before and after the calcination, whereas they are 16.82 Oe and 18.85 Oe for the Fe_3O_4@rGO, respectively. These values show high ferromagnetic properties after the calcination process. In addition, the remnant magnetization values (M_r) for Fe_3O_4 are 2.65 emu/g and 3.73 emu/g before and after the calcination. Similarly, for the Fe_3O_4@rGO NPs, the M_r values are 0.98 emu/g and 3.21 emu/g, respectively. Therefore, as shown in Fig. 8b, by removing organic compounds and increasing the crystallinity of NPs by the calcination process, the magnetization of each particle increased [61,74–77]. Due to being partially coated with reduced graphene oxide, the magnetization of Fe_3O_4@rGO nanoparticles compared to those of Fe_3O_4 is reduced. After the coating with graphene by CVD method and by polymer on graphene-coated MNPs, we expected to decrease the magnetization values of Fe_3O_4@rGO sample. Since the CVD process was done at 950 °C, we obtained Fe-based nanoparticles (BCC Fe and FCC (Fe, C)) due to the high reduction rate. As a characteristic of Fe NPs, Fe-based@rGO@G has a high magnetization compared to that of the Fe_3O_4@rGO, as shown in Fig. 8c. Besides, its coercivity value (H_c) is 402.12 Oe, indicating soft ferromagnetic characteristics of NPs that are utilized in biomedical applications. The magnetization value (M_s) is 139.48 emu/g, and the retentivity value (M_r) is 37.73 emu/g as well (Fig. 8c), which is demonstrated high magnetization value of Fe-based@rGO@G NPs due to Fe content as compared to Fe_3O_4@rGO (Fig. 8b). The coercivity value (H_c), the saturation magnetization value (M_s), and the remnant magnetization value (M_r) after coating with polymer (Fe-based@rGO@G@PMA-POEGMA) are 363.77 Oe, 84.06 emu/g, and 16.64 emu/g, respectively in Fig. 8d. By comparing these results with only graphene-coated MNPs (Fig. 8c), although the

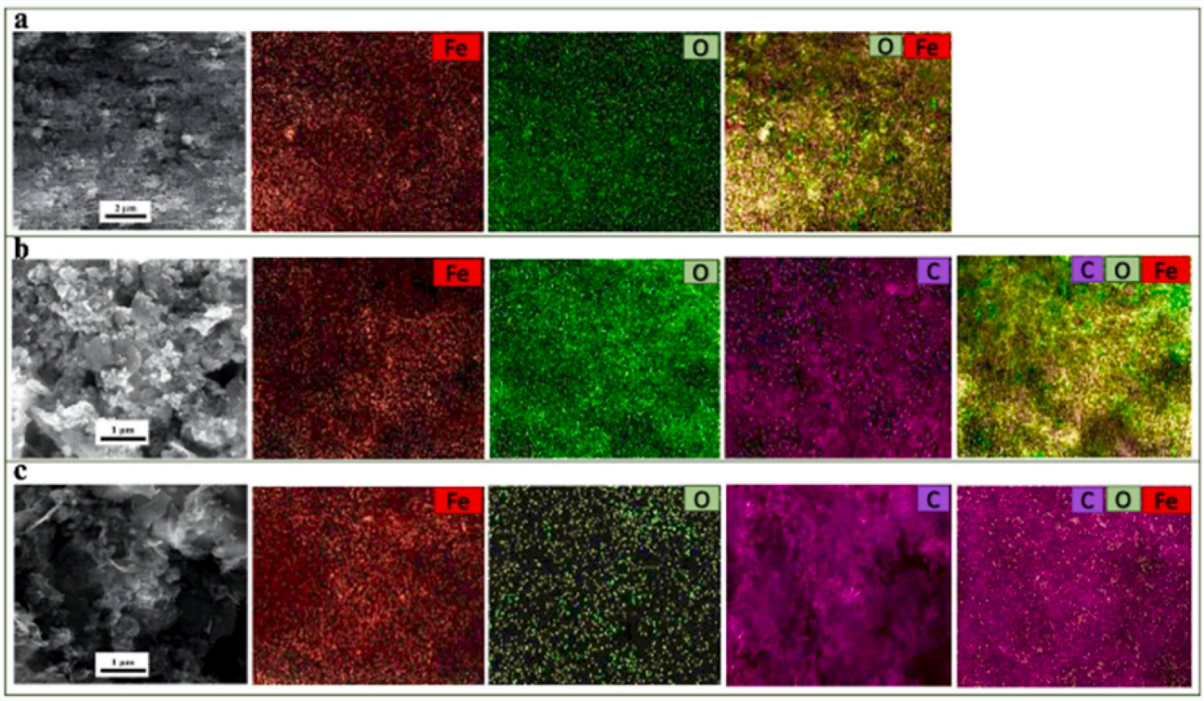


Fig. 9. SEM micrographs and elemental mappings of (a) Fe_3O_4, (b) Fe_3O_4@rGO and (c) Fe-based@rGO@G MNPs.

magnetization decreased, it still demonstrated the soft ferromagnetic properties.

3.4. SEM/TEM analyses

SEM images and elemental mappings (for Fe, C, and O elements) were obtained from solvothermal synthesized NPs before coating and after coating with graphene (Fe_3O_4, Fe_3O_4@rGO, and Fe-based@rGO@G) are presented in Fig. 9a–c. As a result, the distribution of Fe, C, and O is homogeneous in the all nanoparticles. On the other hand, as GO was introduced with the synthesis method and reduced graphene oxide was obtained, the weight of carbon increased from 20.31 wt% to 48.32 wt%, and after coating with graphene, the amount of carbon reached to 85.4 wt%, which shows that all the particles were homogeneously coated with graphene. On the other hand, SEM images cannot show the core-shell structure of NPs due to low magnetization. So, the TEM images and elemental mappings (for Fe, C, and O elements) of Fe_3O_4@rGO and Fe-based@rGO@G are demonstrated in Fig. 10a and b. According to the TEM images, it was confirmed that carbon embedded and partially coated Fe_3O_4 NPs, and it also confirmed the core-shell structure formation of MLG around the Fe_3O_4@rGO NPs, during the high-temperature process. Iron oxide conversion to BCC Fe and FCC (Fe, C) phases in the NPs' structure was approved by the XRD analysis, and a successful synthesis was enabled because the resultant MNPs contain the Fe-based core and the MLG shell. According to these results, a higher magnification image of individual layers of graphene shells with a spacing of ~0.34 nm was observed. Based on former studies of Sıddıka et al. [53], the effect of the CVD processing conditions was found effective in the thickness of the MLG shells. Thus, XRD, Raman, and TEM results indicated that Fe-based MLG encapsulated and rGO embedded magnetic nanoparticles were synthesized successfully.

3.5. BET, ZETA, and DLS analyses

For the size and stability of NPs, DLS and Zeta potential results are demonstrated in Fig. 11. Nanoparticle stability evaluation in the pH 7–8 range is a crucial criterion in assessing their utility in biomedical applications. Thus, Zeta potential measurements in water are used to investigate the aqueous stability of NPs and the efficiency of polymer coatings over nanoparticle surfaces. For the Fe_3O_4 and Fe_3O_4@rGO, the Zeta potential (−13.7 mV and −24.3 mV, given in Fig. S1) and average particle size (112.6 nm and 154.2 nm) were obtained, respectively, which the data depicted in Fig. 11a and b. Also, the Zeta potential (−25.2 mV and −18.2 mV, given in Fig. S1) and particle size (160.3 nm and 136 nm) were obtained, respectively, for the Fe-based@rGO@G and Fe-based@rGO@G@PMA-POEGMA, which are shown in Fig. 11c and d. The Zeta potential due to negative values confirms the stability of all the NPs (Fig. S1). The highest stability is in the graphene-encapsulated iron-based NPs, and by coating with polymer, a significant change occurred in the stability of NPs. The high toxicity of positively charged NPs is explained by their ability to easily enter cells, in contrast to negatively charged and neutral NPs. So, the surface charge is important in deciding whether the nanoparticles will cluster in blood flow or will stick to or interact with oppositely charged cell membranes [71–73]. The plasma and blood cells constantly had a negative charge; NPs with slight negative surface charge can minimize nonspecific contact with these components through electrostatic interactions [71,73,74]. We have all four particles in the mentioned range, which concludes that they are not aggregating and are stable in the conditions in which they are to be used. Moreover, the average particle size of four NPs was shown that no significant changes occurred during the coating of these NPs. Obviously, as shown in Fig. 11d, after polymer coating, the distribution of NPs increases, and the agglomeration decreases from 160.3 nm to 136 nm.

The results of the BET surface area analyses for all samples are given in detail in Table 1, and detailed plots are shown in Fig. S2. It reveals a significant decrease in the pore volume from 0.0693 cm^3/g to 0.0301 cm^3/g upon the embedded of reduced graphene oxide (rGO) within the Fe-based structure. Further encapsulation of Fe_3O_4@rGO with multi-layered graphene markedly decreases the pore volume down to 0.0005 cm^3/g. This decrease in pore volume directly affects the surface area, which diminishes progressively from 214.541 m^2/g to 129.646 m^2/g and further to 56.533 m^2/g. Additionally, N_2 adsorption and desorption isotherms of the samples are given in Fig. S2, as compatible with the decreasing pore volumes [78,79]. This comprehensive analysis

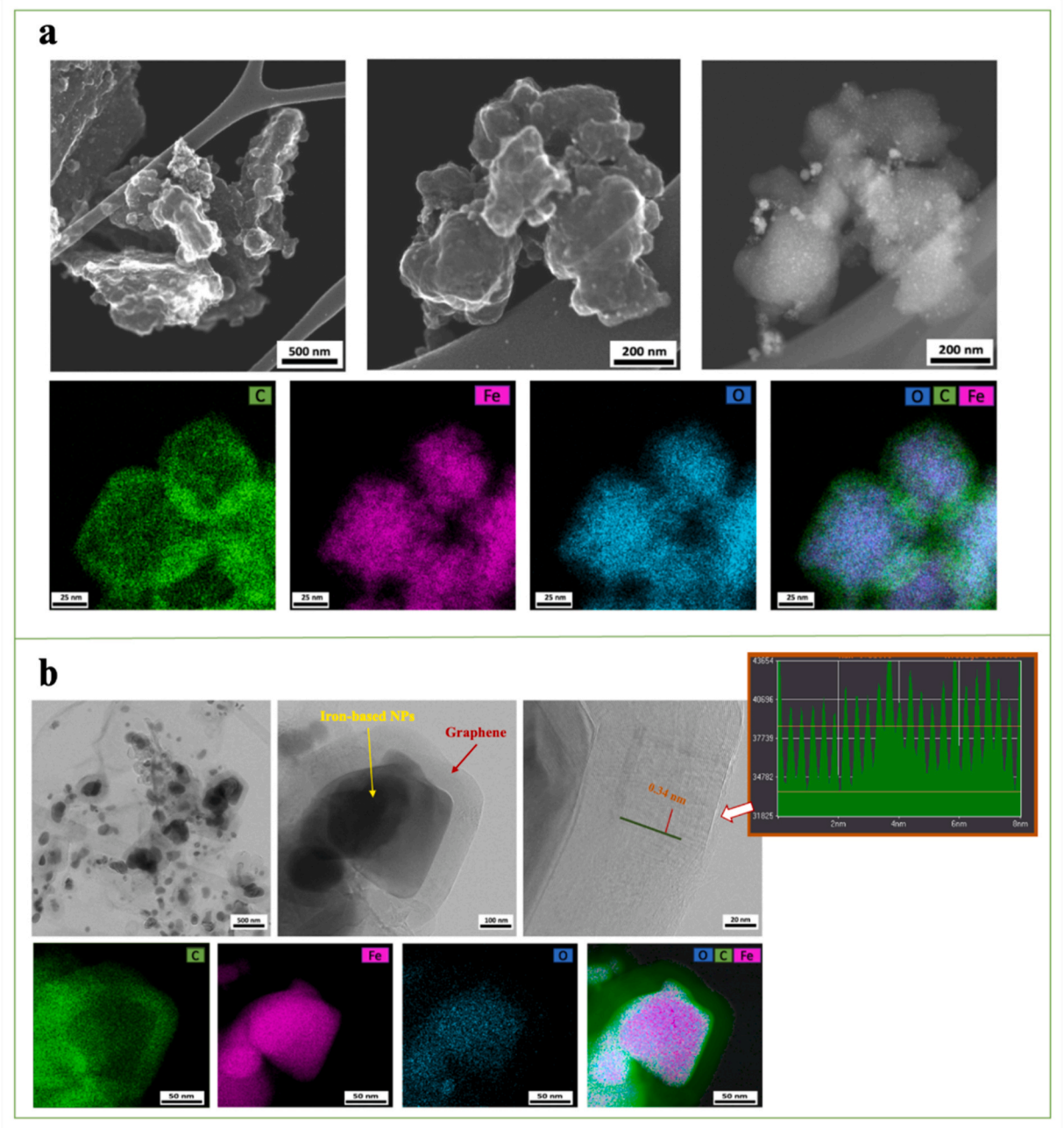


Fig. 10. TEM images and elemental mappings (Fe, C and O elements) of (a) Fe_3O_4@rGO and (b) Fe-based@rGO@G MNPs.

underscores the substantial impact of rGO incorporation and multilayer graphene encapsulation on the Fe_3O_4 nanoparticles, notably affecting their surface area and porosity characteristics.

3.6. ^1H NMR and FTIR analyses

First of all, the pyrene initiator (PyrI) was characterized by a ^1H NMR spectrum, as shown in Fig. 12a. The peaks around 7.9–8.3 ppm were attributed to typical aromatic protons in the pyrene ring. Other characteristic protons were observed at 7–7.1 ppm (*N–H*), 5.2 ppm (-CH_2-), and 1.9–2.1 ppm (-CH_3). The chemical structure of PMA-POEGMA was confirmed by ^1H NMR analysis in $CDCl_3$, as seen from the NMR spectrum Fig. 12b. The signals around 8.0–8.2 ppm were attributed to aromatic protons of the pyrene moiety. As seen in Fig. 12, all other typical proton signals in the structure of PMA-POEGMA were observed around 5–5.3 ppm (a), 3.6–3.8 ppm (b and c), 3.3–3.4 ppm (d), 1.6–2 ppm (e) and 0.7–1.1 ppm (g and f), respectively [80].

FTIR spectra of the Fe-based@rGO@G@PMA-POEGMA obtained using polymers with different amounts (5 mg, 10 mg, and 50 mg) are shown in Fig. 13b. Three characteristic absorption bands were observed in the FTIR spectra of MNPs at 1109 cm^{-1} (*C*–O stretching), 1725 cm^{-1} (C═O stretching), and 2870 cm^{-1} (*C*–H stretching) [81]. Considering the feed ratio of PMA-POEGMA for coating (5 mg–50 mg), the peak intensities were directly increased with increasing amounts of PMA-POEGMA. These results confirmed that multi-layered graphene-encapsulated iron-based MNPs were successfully coated with PMA-POEGMA. Photographic images of a colloidal mixture of the nanoparticles with different concentrations are displayed in Fig. 13a. As shown, the precipitation behavior of the MNPs by increasing the polymer concentration was reduced from 100% to 30% for 24 h and, as a result, the colloidal stability increased over time.

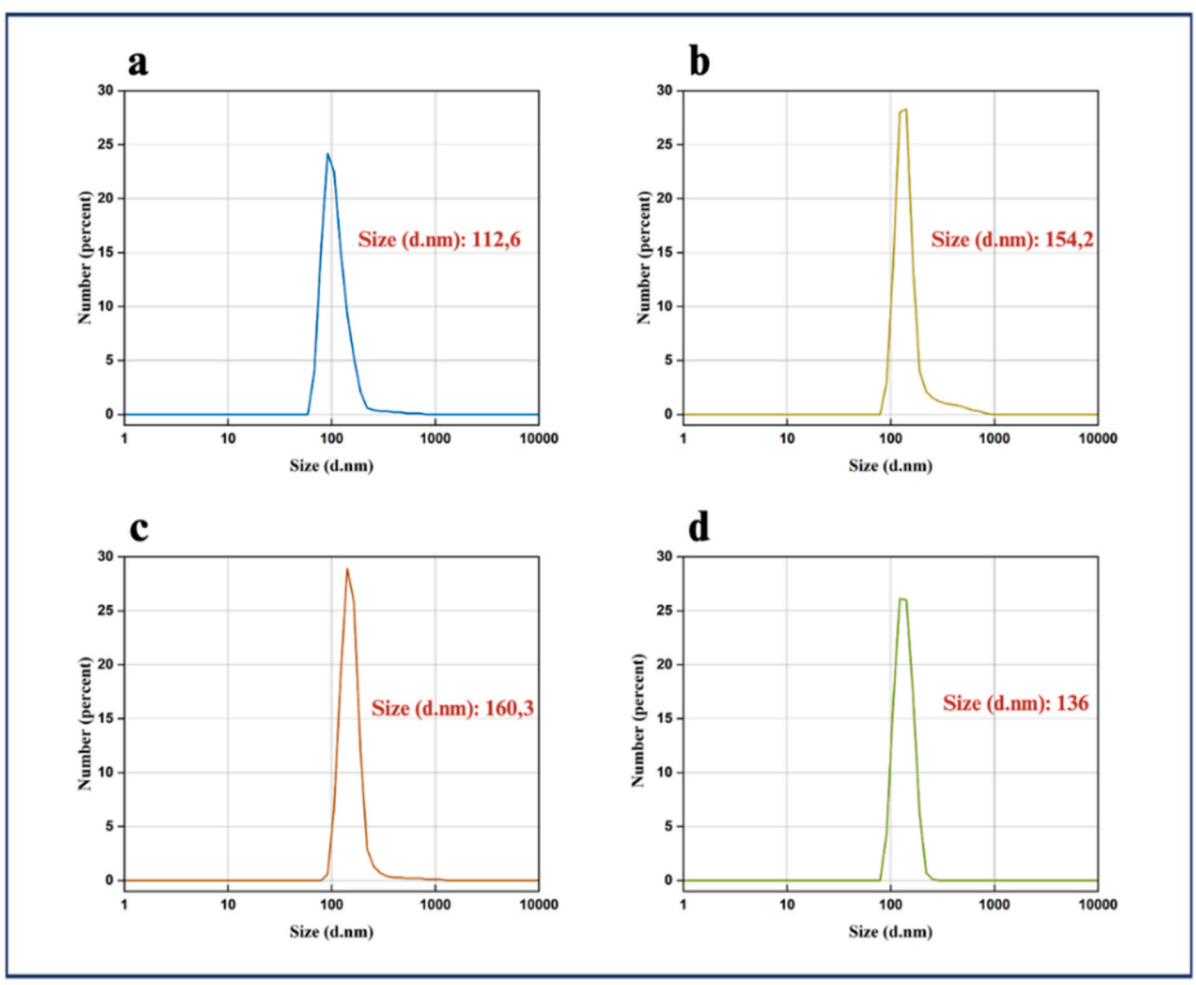


Fig. 11. DLS analyses of (a) Fe_3O_4, (b) Fe_3O_4@rGO, (c) Fe-based@rGO@G, and (d) Fe-based@rGO@G@PMA-POEGMA MNPs.

Table 1
BET measurements of Fe_3O_4, Fe_3O_4@rGO and Fe/Fe_3C@rGO@G nanoparticles.

Samples	BET Surface Area (m^2/g)	Pore Size Adsorption/Desorption	Pore Volume (cm^3/g)
Fe_3O_4	214.541	16.72 nm/10.34 nm	0.0693
Fe_3O_4@rGO	129.646	20.10 nm/13.79 nm	0.0301
Fe-based@rGO@G	56.533	19.39 nm/13.59 nm	0.0005

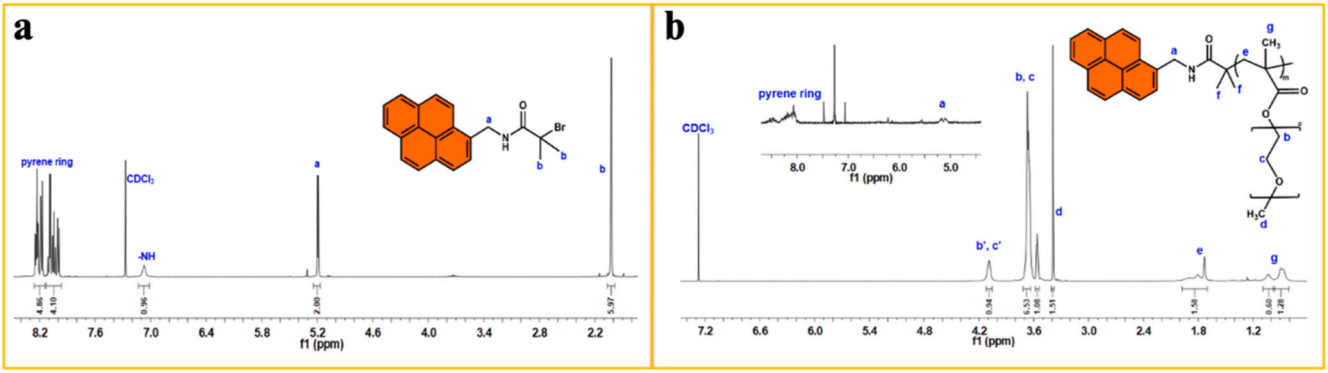


Fig. 12. (a) ^1H NMR spectrum of Pyrene initiator (PyrI), and (b) PMA-POEGMA.

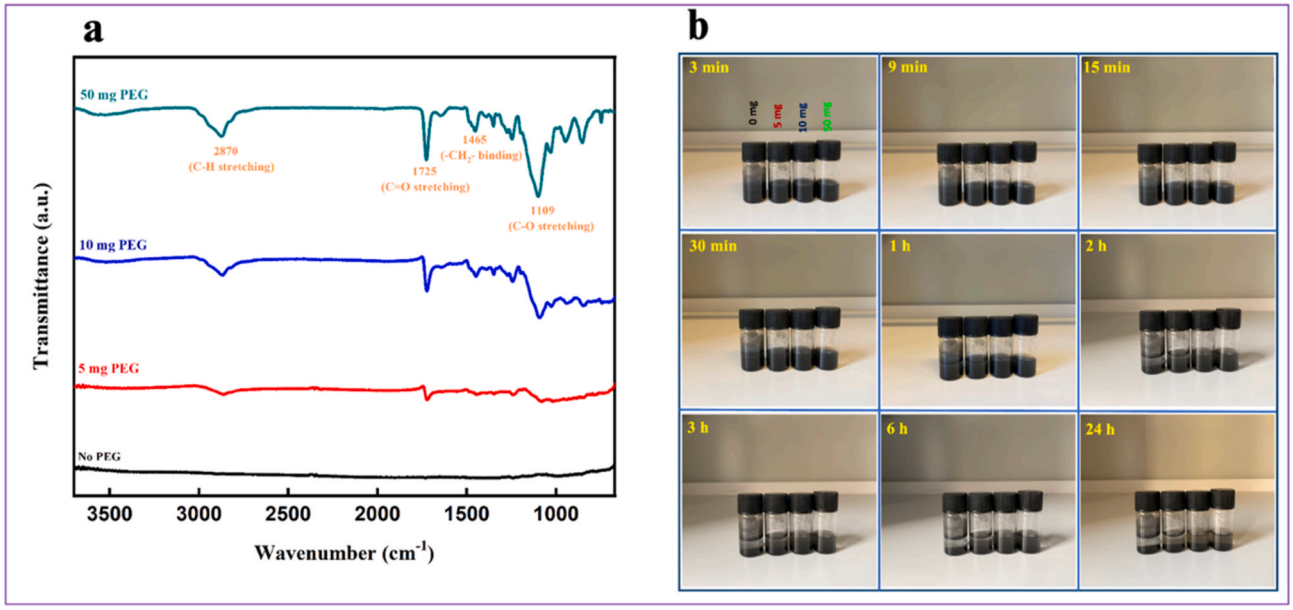


Fig. 13. FTIR spectra of (a) 0 mg, 5 mg, 10 mg and 50 mg PMA-POEGMA coated Fe-based@rGO@G MNPs, and (b) precipitation images of Fe-based@rGO@G@PMA-POEGMA MNPs dependent to time.

3.7. Cytotoxicity evaluation

The possible cytotoxic effect of the MNPs was investigated by MTT assay for 72 h. To do this, MCF-7 breast cancer cells were selected as models since it is the most studied breast cancer cell line in the world [82]. Because experimental errors were observed in the initial experiments due to the precipitation of MNPs at the bottom of the assay plate functioning as a barrier for light to pass through, no-cell control was also used in addition to DMSO control. When deciding on dosages to be applied, we considered similar studies [83,84] and decided on a range between 5×10^{-5} μg/mL and 5×10^{2} μg/mL in order to be able to scan a wide dose area.

In cells treated with Fe_3O_4 nanoparticles, treatment with a higher concentration than 5×10^{-2} μg/mL NPs for 6 h resulted in cell proliferation, but recovery was observed in further incubation periods, and cell viability returned to the control group level. Cell viability was observed as similar to the control group upon treatment for 24 h, 30 h, or 48 h. Cell viability was observed as ~70% even at the highest dosages after 72 h treatment, which indicates that Fe_3O_4 nanoparticles are not toxic to MCF-7 cells up to 48 h even at the highest dose applied, and only slight cytotoxicity was observed in further incubation periods in Fig. 14a. In cells treated with rGO coated Fe_3O_4 nanoparticles (Fe_3O_4@rGO), significant alteration in cytotoxicity was not observed in cells treated with nanoparticles for up to 48 h, although slight proliferation was observed in cells treated for up to 30 h 48 h treatment did not affect cell viability while treatment for 72 h resulted in dose-dependent cytotoxicity. Half of the cells were observed as dead upon 5×10^{2} μg/mL treatment for 72 h in Fig. 14b. Treatment of MCF-7 cells with Fe-based@rGO@G@PMA-POEGMA nanoparticles decreased cell viability in a dose-dependent manner but treatment with higher concentration than 5×10^{-2} μg/mL for 6 h increased cell viability up to 10%, which was recovered in longer incubation period in Fig. 14c. The cytotoxic effect of nanoparticles varies depending on various factors, including chemical composition, size, shape, surface charge, and concentration [85]. According to the study by Jano et al. [86], the combination of MNPs with doxorubicin, significantly inhibited breast cancer cell growth and proliferation compared to doxorubicin alone, indicating their potential to enhance therapeutic efficacy while minimizing side effects. Although coating of Fe_3O_4 nanoparticles changes their characteristics, the response of MCF-7 cells to MNP treatment for up to 48 h resembles each other, while treatment of Fe_3O_4@rGO or Fe-based@rGO@G@PMA-POEGMA for 72 h reduces cell viability in a dose-dependent manner up to 50%. Thus, by considering these nanoparticles as drug carriers, all nanoparticles tested were accepted as suitable. However Fe-based@rGO@G@PMA-POEGMA was observed as the most promising one.

4. Conclusion

In this study, Fe_3O_4, Fe_3O_4@rGO, Fe-based@rGO@G, and its PMA-POEGMA coated form were successfully synthesized using solvothermal synthesis, chemical vapor deposition, and purification methods. Soft ferromagnetic (M_s: 84.06 emu/g; H_c: 363.77 Oe for Fe-based@rGO@G@PMA-POEGMA) nanoparticles (~136 nm) with high specific surface area (~60 m^2/g) were obtained for potential usage in biomedical applications. Recognizing the critical role of chemical stability in the functionality and biocompatibility of magnetic nanoparticles, efforts were made to enhance their chemical stability to withstand challenges in biological environments. Coating the MNPs with multi-layered graphene via chemical vapor deposition and subsequent purification treatments improved their magnetic properties and stability. Further modifications with a PEG-based polymer aimed to enhance dispersion properties and biocompatibility. Characterization techniques and cytotoxicity assessments highlighted the potential of these multi-layered graphene and PEG encapsulated magnetic nanoparticles for biomedical applications. Cell viability of the magnetic nanoparticles could be in the order of 50% even if a high incubation time, such as 72 h, is applied. Thus, due to their favorable characteristics, concentrations up to 500 μg/mL during short incubation time can be utilized particularly in drug delivery.

CRediT authorship contribution statement

Aysa Azmoudeh: Writing – original draft, Investigation, Formal analysis. **Sencer Moral:** Investigation. **Seyma Sari:** Writing – original draft, Investigation. **Miray Türk:** Writing – original draft, Investigation. **Muhammet U. Kahveci:** Writing – original draft, Methodology. **Gizem Dinler Doganay:** Writing – original draft, Methodology. **Duygu Ağaoğulları:** Writing – original draft, Supervision, Project administration, Conceptualization.

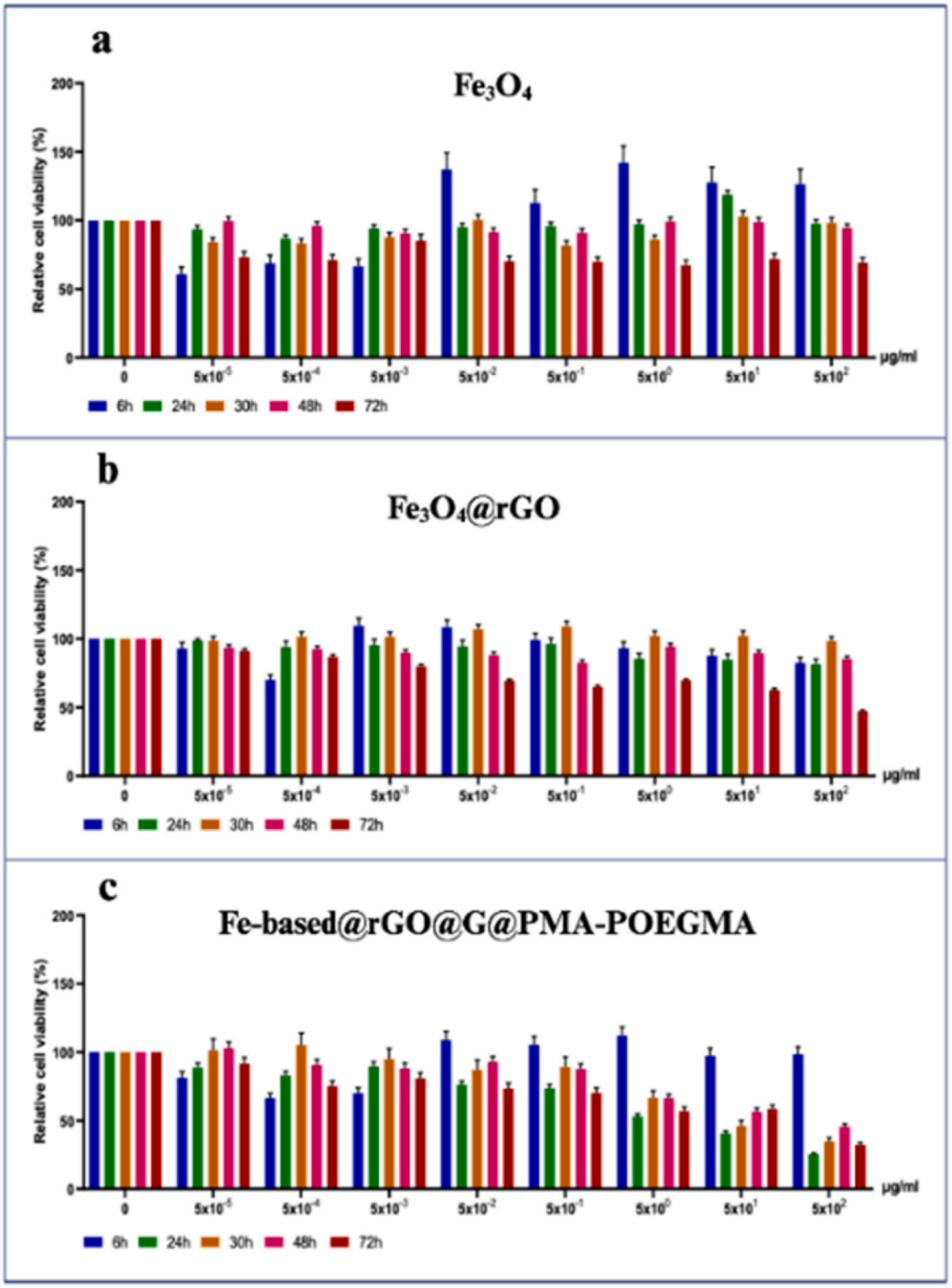


Fig. 14. Cytotoxicity evaluation of Fe-based MNPs on MCF-7 cells treated by different concentrations (5×10^{-5} µg/mL to 5×10^{2} µg/mL) of each NP for up to 72 h. (a) effect of Fe_3O_4 MNPs of MCF-7 cell viability, (b) effect of Fe_3O_4@rGO nanoparticles of MCF-7 cell viability, (c) effect of Fe-based@rGO@G@PMA-POEGMA nanoparticles of MCF-7 cell viability.

Declaration of competing interest

The authors declare that they have no known competing financial interests or personal relationships that could have appeared to influence the work reported in this paper.

Acknowledgments

This study was supported by the Scientific Research Projects Department of Istanbul Technical University, with the project number of MDA-2022-43611 (ITU BAP/DAP Project). We express our gratitude to Asst. Prof. Dr. Murat Kuscu from Koc University for his invaluable support in all characterization analyses, and Dr. Sedat Kurnaz from Kastamonu University for conducting the VSM analyses. We also extend our thanks to KUYTAM for their assistance with XPS and BET analyses and to KUBAM for their help with DTA/TG analyses. Additionally, we appreciate the help from Koç University Nanofabrication and Nanocharacterization Center (n2star) for the TEM analysis.

Appendix A. Supplementary data

Supplementary data to this article can be found online at https://doi.org/10.1016/j.jsamd.2024.100776.

References

[1] H.D.T. Duong, D.T. Nguyen, K.S. Kim, Effects of process variables on properties of CoFe2O4 nanoparticles prepared by solvothermal process, Nanomaterials 11 (2021), https://doi.org/10.3390/nano11113056.

[2] A. Mittal, I. Roy, S. Gandhi, Magnetic nanoparticles: an overview for biomedical applications, Magnetochemistry. 8 (2022), https://doi.org/10.3390/magnetochemistry8090107.

[3] Y.A. Koksharov, S.P. Gubin, I.V. Taranov, G.B. Khomutov, Y.V. Gulyaev, Magnetic nanoparticles in medicine: progress, problems, and advances, J. Commun. Technol. Electron. 67 (2022) 101–116, https://doi.org/10.1134/S1064226922020073.

[4] E.K. Schneider-Futschik, F. Reyes-Ortega, Pharmaceutics Advantages and Disadvantages of Using Magnetic Nanoparticles for the Treatment of Complicated Ocular Disorders, vol. 13, 2021, https://doi.org/10.3390/pharmaceutics.

[5] H. Shen, J. Hou, Z. Gao, B. Chen, T. Tan, Solvothermal synthesis of functional magnetic nanoparticles for biocatalyst, Appl. Biochem. Biotechnol. 173 (2014) 2279–2286, https://doi.org/10.1007/s12010-014-1033-9.

[6] C. Cháfer-Pericás, A. Maquieira, R. Puchades, Functionalized inorganic nanoparticles used as labels in solid-phase immunoassays, TrAC, Trends Anal. Chem. 31 (2012) 144–156, https://doi.org/10.1016/j.trac.2011.07.011.

[7] M. Bustamante-Torres, D. Romero-Fierro, J. Estrella-Nuñez, B. Arcentales-Vera, E. Chichande-Proaño, E. Bucio, S. José, P. Yachay, Polymeric composite of magnetite iron oxide nanoparticles and their application in biomedicine: a review, Polymers 14 (2022), https://doi.org/10.3390/polym.

[8] M.R.Z. Kouhpanji, B.J.H. Stadler, A guideline for effectively synthesizing and characterizing magnetic nanoparticles for advancing nanobiotechnology: a review, Sensors (Switzerland) 20 (2020), https://doi.org/10.3390/s20092554.

[9] F. Ozel, H. Kockar, A simple method of synthesis and characterizations of oleate-coated iron oxide nanoparticles, J. Supercond. Nov. Magnetism 30 (2017) 2023–2027, https://doi.org/10.1007/s10948-016-3844-0.

[10] W. Li, P. Xu, H. Zhou, L. Yang, H. Liu, Advanced functional nanomaterials with microemulsion phase, Sci. China Technol. Sci. 55 (2012) 387–416, https://doi.org/10.1007/s11431-011-4687-3.

[11] A.K. Ganguli, A. Ganguly, S. Vaidya, Microemulsion-based synthesis of nanocrystalline materials, Chem. Soc. Rev. 39 (2010) 474–485, https://doi.org/10.1039/b814613f.

[12] I. Morjan, R. Alexandrescu, F. Dumitrache, C. Fleaca, R. Birjega, I. Soare, C. R. Luculescu, V. Prodan, V. Kuncser, G. Filoti, H. Xu, D. Wang, Development of magnetic Fe@C nanocomposites obtained via the laser pyrolysis: structural and disaggregation properties, in: AIP Conf Proc, 2010, pp. 17–21, https://doi.org/10.1063/1.3505074.

[13] S. Veintemillas-Verdaguer, O. Bomat I I-Miguel, M.P. Morales, Effect of the process conditions on the structural and magnetic properties of c-Fe 2 O 3 nanoparticles produced by laser pyrolysis, Scripta Mater. 47 (2002) 589–593, https://doi.org/10.1016/S1359-6462(02)00198-7.

[14] J.C. De Freitas, R.M. Branco, I.G.O. Lisboa, T.P. Da Costa, M.G.N. Campos, M. J. Júnior, R.F.C. Marques, Magnetic nanoparticles obtained by homogeneous coprecipitation sonochemically assisted, in: Materials Research, Universidade Federal de Sao Carlos, 2015, pp. 220–224, https://doi.org/10.1590/1516-1439.366114.

[15] S.J. Shin, Y.H. Kim, C.W. Kim, H.G. Cha, Y.J. Kim, Y.S. Kang, Preparation of magnetic FeCo nanoparticles by coprecipitation route, Curr. Appl. Phys. 7 (2007) 404–408, https://doi.org/10.1016/j.cap.2006.09.012.

[16] L. Yang, P. Zou, J. Cao, Y. Sun, D. Han, S. Yang, G. Chen, X. Kong, J. Yang, Facile synthesis and paramagnetic properties of Fe3O4@SiO2 core-shell nanoparticles, Superlattice. Microst. 76 (2014) 205–212, https://doi.org/10.1016/j.spmi.2014.10.011.

[17] C. Wang, D. Astruc, Recent developments of metallic nanoparticle-graphene nanocatalysts, Prog. Mater. Sci. 94 (2018) 306–383, https://doi.org/10.1016/j.pmatsci.2018.01.003.

[18] C.C. Berry, Progress in functionalization of magnetic nanoparticles for applications in biomedicine, J. Phys. D Appl. Phys. 42 (2009), https://doi.org/10.1088/0022-3727/42/22/224003.

[19] S. Roth, M. Margulis, A. Danielli, Recent advances in rapid and highly sensitive detection of proteins and specific DNA sequences using a magnetic modulation biosensing system, Sensors 22 (2022), https://doi.org/10.3390/s22124497.

[20] K. Yasuda, Y. Kitamoto, Fabrication of Fe3O4 nanorods designed for liquid-phase magnetic biosensing, in: AIP Conf Proc, American Institute of Physics Inc., 2018, https://doi.org/10.1063/1.5021922.

[21] H. Fatima, T. Charinpanitkul, K.S. Kim, Fundamentals to apply magnetic nanoparticles for hyperthermia therapy, Nanomaterials 11 (2021), https://doi.org/10.3390/nano11051203.

[22] M. Peiravi, H. Eslami, M. Ansari, H. Zare-Zardini, Magnetic hyperthermia: potentials and limitations, J. Indian Chem. Soc. 99 (2022), https://doi.org/10.1016/j.jics.2021.100269.

[23] A. Rajan, N.K. Sahu, Review on magnetic nanoparticle-mediated hyperthermia for cancer therapy, J. Nanoparticle Res. 22 (2020), https://doi.org/10.1007/s11051-020-05045-9.

[24] E. Baco, O. Ukimura, E. Rud, L. Vlatkovic, A. Svindland, M. Aron, S. Palmer, T. Matsugasumi, A. Marien, J.C. Bernhard, J.C. Rewcastle, H.B. Eggesbø, I.S. Gill, Magnetic resonance imaging-transectal ultrasound image-fusion biopsies accurately characterize the index tumor: correlation with step-sectioned radical prostatectomy specimens in 135 patients, Eur. Urol. 67 (2015) 787–794, https://doi.org/10.1016/j.eururo.2014.08.077.

[25] L. Yin, W. Li, Y. Du, K. Wang, Z. Liu, H. Hui, J. Tian, Recent developments of the reconstruction in magnetic particle imaging, Vis Comput Ind Biomed Art. 5 (2022), https://doi.org/10.1186/s42492-022-00120-5.

[26] X. Yang, G. Shao, Y. Zhang, W. Wang, Y. Qi, S. Han, H. Li, Applications of magnetic particle imaging in biomedicine: advancements and prospects, Front. Physiol. 13 (2022), https://doi.org/10.3389/fphys.2022.898426.

[27] X. Ke, X. Song, N. Qin, Y. Cai, F. Ke, Rational synthesis of magnetic Fe 3 O 4 @MOF nanoparticles for sustained drug delivery, J. Porous Mater. 26 (2019) 813–818, https://doi.org/10.1007/s10934-018-0682-4.

[28] Manuel Arruebo, Rodrigo Fernández-Pacheco, M. Ricardo Ibarra, Jesús Santamaría, Magnetic nanoparticles for drug delivery, Nano Today 2 (2007) 22–32, https://doi.org/10.1016/S1748-0132(07)70084-1.

[29] H.M. Williams, The application of magnetic nanoparticles in the treatment and monitoring of cancer and infectious diseases, Bioscience. Horizons.: Int. J. Stud. Res. 10 (2017), https://doi.org/10.1093/biohorizons/hzx009.

[30] H. Chen, F. Liu, Z. Lei, L. Ma, Z. Wang, Fe2O3@Au core@shell nanoparticle-graphene nanocomposites as theranostic agents for bioimaging and chemo-photothermal synergistic therapy, RSC Adv. 5 (2015) 84980–84987, https://doi.org/10.1039/c5ra17143a.

[31] A. Dobranici, A. Șelaru, E. Olăreț, I. Stancu, M. Costache, S. Dinescu, MNPs-Enriched Biomaterials as Promising Candidates for Nervous Tissue Engineering Applications, MDPI AG, 2022, p. 7, https://doi.org/10.3390/materproc2022009007.

[32] Z. Liu, J. Liu, X. Cui, X. Wang, L. Zhang, P. Tang, Recent advances on magnetic sensitive hydrogels in tissue engineering, Front. Chem. 8 (2020), https://doi.org/10.3389/fchem.2020.00124.

[33] B. Pérez-López, A. Merkoçi, Carbon nanotubes and graphene in analytical sciences, Microchim. Acta 179 (2012) 1–16, https://doi.org/10.1007/s00604-012-0871-9.

[34] C. Qiu, K.E. Bennet, T. Khan, J.D. Ciubuc, F.S. Manciu, Raman and conductivity analysis of graphene for biomedical applications, Materials 9 (2016) 1–12, https://doi.org/10.3390/ma9110897.

[35] V. Kumar, A. Kumar, D.J. Lee, S.S. Park, Estimation of number of graphene layers using different methods: a focused review, Materials 14 (2021) 1–22, https://doi.org/10.3390/ma14164590.

[36] A. Geim, K. Novoselov, The rise of graphene, Nat. Mater. 6 (2007) 183–191, https://doi.org/10.1038/nmat1849.

[37] A. Garanina, I. Kireev, O. Zhironkina, O. Strelkova, A. Shakhov, I. Alieva, V. Davydov, S. Murugesan, V. Khabashesku, A. Majouga, V. Agafonov, R. Uzbekov, Long-term live cells observation of internalized fluorescent Fe@C nanoparticles in constant magnetic field, J. Nanobiotechnol. 17 (2019), https://doi.org/10.1186/s12951-019-0463-5.

[38] W.J. Han, S.H. Piao, H.J. Choi, Y. Seo, Core–shell structured mesoporous magnetic nanoparticles and their magnetorheological response, Colloids Surf. A Physicochem. Eng. Asp. 524 (2017) 79–86, https://doi.org/10.1016/j.colsurfa.2017.04.016.

[39] L. Zhao, X. Dai, B. Li, H. Wang, H. Li, C. Liang, Synthesis and characterization of flower-like carbon-encapsulated Fe-C nanoparticles for application as adsorbing material, Materials 12 (2019), https://doi.org/10.3390/MA12050829.

[40] C. Cui, W. Qian, C. Zheng, Y. Liu, S. Yun, Y. Yu, J. Nie, F. Wei, Formation mechanism of carbon encapsulated Fe nanoparticles in the growth of single-/double-walled carbon nanotubes, Chem. Eng. J. 223 (2013) 617–622, https://doi.org/10.1016/j.cej.2013.03.039.

[41] A.A. El-Gendy, E.M.M. Ibrahim, V.O. Khavrus, Y. Krupskaya, S. Hampel, A. Leonhardt, B. Büchner, R. Klingeler, The synthesis of carbon coated Fe, Co and Ni nanoparticles and an examination of their magnetic properties, Carbon 47 (2009) 2821–2828, https://doi.org/10.1016/j.carbon.2009.06.025.

[42] M.M. Lima, D.L.P. Macuvele, L. Muller, J. Nones, L.L. Silva, M.A. Fiori, C. Soares, H.G. Riella, Synthesis and potential adsorption of Fe3O4@ C core-shell nanoparticles for to removal of pollutants in aqueous solutions: a brief review, J. Adv. Chem. Eng. 7 (2017), https://doi.org/10.4172/2090-4568.1000172.

[43] H. Cao, G. Huang, S. Xuan, Q. Wu, F. Gu, C. Li, Synthesis and characterization of carbon-coated iron core/shell nanostructures, J. Alloys Compd. 448 (2008) 272–276, https://doi.org/10.1016/j.jallcom.2006.10.019.

[44] L. Fu, M.G. Humphrey, C. Zhang, Covalent edge-functionalization of graphene oxide with porphyrins for highly efficient photoinduced electron/energy transfer and enhanced nonlinear optical performance, Nano Res. 16 (2023) 25–32, https://doi.org/10.1007/s12274-022-4729-0.

[45] S. Song, C. Wan, Y. Zhang, Non-covalent functionalization of graphene oxide by pyrene-block copolymers for enhancing physical properties of poly(methyl methacrylate), RSC Adv. 5 (2015) 79947–79955, https://doi.org/10.1039/c5ra14967c.

[46] I.A. Vacchi, C. Ménard-Moyon, A. Bianco, Chemical functionalization of graphene family members, Phys. Sci. Rev. 2 (2017), https://doi.org/10.1515/psr-2016-0103.

[47] B. Zhong, A. Mateu-Roldán, M.L. Fanarraga, W. Han, D. Muñoz-Guerra, J. González, L. Tao Weng, M. Ricardo Ibarra, C. Marquina, K. Lun Yeung, Graphene-encapsulated magnetic nanoparticles for safe and steady delivery of ferulic acid in diabetic mice, Chem. Eng. J. 435 (2022), https://doi.org/10.1016/j.cej.2021.134466.

[48] C. Wen, R. Cheng, T. Gong, Y. Huang, D. Li, X. Zhao, B. Yu, D. Su, Z. Song, W. Liang, β-Cyclodextrin-cholic acid-hyaluronic acid polymer coated Fe3O4-graphene oxide nanohybrids as local chemo-photothermal synergistic agents for enhanced liver tumor therapy, Colloids Surf. B Biointerfaces 199 (2021), https://doi.org/10.1016/j.colsurfb.2020.111510.

[49] M. Szekeres, I.Y. Tóth, E. Illés, A. Hajdú, I. Zupkó, K. Farkas, G. Oszlánczi, L. Tiszlavicz, E. Tombácz, Chemical and colloidal stability of carboxylated core-

shell magnetite nanoparticles designed for biomedical applications, Int. J. Mol. Sci. 14 (2013) 14550–14574, https://doi.org/10.3390/ijms140714550.
[50] S.W. Hong, K.H. Kim, J. Huh, C.H. Ahn, W.H. Jo, Design and synthesis of a new pH sensitive polymeric sensor using fluorescence resonance energy transfer, Chem. Mater. 17 (2005) 6213–6215, https://doi.org/10.1021/cm051663o.
[51] J. Ding, L. Cheng, X. Zhuang, Three-dimensional hierarchical structured Fe3O4/rGO/ZnO composite for effective electromagnetic wave absorption, Appl. Phys. Mater. Sci. Process 127 (2021), https://doi.org/10.1007/s00339-021-04625-3.
[52] A. Alkhayal, A. Fathima, A.H. Alhasan, E.H. Alsharaeh, Peg coated Fe3O4/RGO nano-cube-like structures for cancer therapy via magnetic hyperthermia, Nanomaterials 11 (2021), https://doi.org/10.3390/nano11092398.
[53] S. Mertdinç-Ülküseven, U. Savaci, K. Onbasli, Ö. Balci-Çagiran, H.Y. Acar, M. L. Öveçoglu, D. Agaogullari, In-situ synthesis of graphene encapsulated Fe/Fe2O3nanoparticles for possible biomedical applications, J. Mater. Res. Technol. 20 (2022) 2558–2577, https://doi.org/10.1016/j.jmrt.2022.08.059.
[54] Z. Vasiljević, M.P. Dojčinović, J.D. Vujančević, M. Spreitzer, J. Kovač, D. Bartolić, S. Marković, I. Janković-Častvan, N.B. Tadić, M.V. Nikolić, Exploring the impact of calcination parameters on the crystal structure, morphology, and optical properties of electrospun Fe2TiO5nanofibers, RSC Adv. 11 (2021) 32358–32368, https://doi.org/10.1039/d1ra05748k.
[55] I.P. Grudzinski, M. Bystrzejewski, P. Bogorodzki, A. Cieszanowski, W. Szeszkowski, M. Poplawska, M. Bamburowicz-Klimkowska, Comprehensive magnetic resonance characteristics of carbon-encapsulated iron nanoparticles: a new frontier for the core-shell–type contrast agents, J. Nanoparticle Res. 22 (2020) 1–17, https://doi.org/10.1007/s11051-020-04795-w.
[56] M. Bystrzejewski, K. Pyrzyńska, A. Huczko, H. Lange, Carbon-encapsulated magnetic nanoparticles as separable and mobile sorbents of heavy metal ions from aqueous solutions, Carbon 47 (2009) 1201–1204, https://doi.org/10.1016/j.carbon.2009.01.007.
[57] D. Ağaoğulları, S.J. Madsen, B. Ögüt, A.L. Koh, R. Sinclair, Synthesis and characterization of graphite-encapsulated iron nanoparticles from ball milling-assisted low-pressure chemical vapor deposition, Carbon 124 (2017) 170–179, https://doi.org/10.1016/j.carbon.2017.08.043.
[58] M. Mirza-Aghayan, M. Molaee Tavana, R. Boukherroub, Sulfonated reduced graphene oxide as a highly efficient catalyst for direct amidation of carboxylic acids with amines using ultrasonic irradiation, Ultrason. Sonochem. 29 (2016) 371–379, https://doi.org/10.1016/j.ultsonch.2015.10.009.
[59] S. Saha, M. Jana, P. Samanta, N. Chandra Murmu, N.H. Kim, T. Kuila, J.H. Lee, Hydrothermal synthesis of Fe3O4/RGO composites and investigation of electrochemical performances for energy storage applications, RSC Adv. 4 (2014) 44777–44785, https://doi.org/10.1039/c4ra07388f.
[60] R. Hatel, S. El Majdoub, A. Bakour, M. Khenfouch, M. Baitoul, Graphene oxide/Fe3O4 nanorods composite: structural and Raman investigation, in: J Phys Conf Ser, Institute of Physics Publishing, 2018, https://doi.org/10.1088/1742-6596/1081/1/012006.
[61] Y.P. Yew, K. Shameli, M. Miyake, N.B. Bt Ahmad Khairudin, S.E. Bt Mohamad, H. Hara, M.F. Bt Mad Nordin, K.X. Lee, An eco-friendly means of biosynthesis of superparamagnetic magnetite nanoparticles via marine polymer, IEEE Trans. Nanotechnol. 16 (2017) 1047–1052, https://doi.org/10.1109/TNANO.2017.2747088.
[62] Q. Yan, J. Li, X. Zhang, J. Zhang, Z. Cai, In situ formation of graphene-encapsulated iron nanoparticles in carbon frames through catalytic graphitization of kraft lignin, Nanomater. Nanotechnol. 8 (2018), https://doi.org/10.1177/1847980418818955.
[63] G. Yang, H.Y. Kim, S. Jang, J. Kim, Transfer-free growth of multilayer graphene using self-assembled monolayers, ACS Appl. Mater. Interfaces 8 (2016) 27115–27121, https://doi.org/10.1021/acsami.6b08974.
[64] J.H. Kim, H.S. Kim, S.H. Kim, Aerosol growth and photothermal ignition of multilayer graphene-encapsulated nickel nanoparticles, Powder Technol. 364 (2020) 522–530, https://doi.org/10.1016/j.powtec.2020.02.023.
[65] H.I. Chu, H.Y. Ho, Y.J. Huang, D.S. Tsai, C.P. Lee, Synthesis of non-planar graphene-wrapped copper nanoparticles with iron(III) oxide decoration for high performance supercapacitors, Nanotechnology 34 (2023), https://doi.org/10.1088/1361-6528/acca8a.
[66] G. Vinodhkumar, J. Wilson, S.S.R. Inbanathan, I.V. Potheher, M. Ashokkumar, A. C. Peter, Solvothermal synthesis of magnetically separable reduced graphene oxide/Fe3O4 hybrid nanocomposites with enhanced photocatalytic properties, Phys. B Condens. Matter 580 (2020), https://doi.org/10.1016/j.physb.2019.411752.
[67] Y. Li, N. Chopra, Fabrication of nanoscale heterostructures comprised of graphene-encapsulated gold nanoparticles and semiconducting quantum dots for photocatalysis, Phys. Chem. Chem. Phys. 17 (2015) 12881–12893, https://doi.org/10.1039/c5cp00928f.
[68] D. Zhou, T.L. Zhang, B.H. Han, One-step solvothermal synthesis of an iron oxide-graphene magnetic hybrid material with high porosity, Microporous Mesoporous Mater. 165 (2013) 234–239, https://doi.org/10.1016/j.micromeso.2012.08.011.
[69] F.G. Mendonça, J.D. Ardisson, R.M. Lago, J.C. Tristão, Selective oxidation of amorphous carbon by CO2 to produce Fe@C nanoparticles from bulky Fe/C matrices, J. Braz. Chem. Soc. 26 (2015) 2379–2383, https://doi.org/10.5935/0103-5053.20150212.
[70] S.H. Dhawane, T. Kumar, G. Halder, Parametric effects and optimization on synthesis of iron (II) doped carbonaceous catalyst for the production of biodiesel, Energy Convers. Manag. 122 (2016) 310–320, https://doi.org/10.1016/j.enconman.2016.06.005.
[71] A. Sukhanova, S. Bozrova, P. Sokolov, et al., Dependence of nanoparticle toxicity on their physical and chemical properties, Nanoscale Res. Lett. 13 (2018) 1–21, https://doi.org/10.1186/s11671-018-2457-x.
[72] N. Chandrasekar, K. Mohan Kumar, K. Selvan Balasubramnian, R. Varadharajan, Facile synthesis of iron oxide, iron-cobalt and zero valent iron nanoparticles and evaluation of their anti microbial activity, free radicle SCAVENGINGING activity and antioxidant assay, n.d. Digest Journal of Nanomaterials & Biostructures (DJNB) 8 (2) (2013) 765–775.
[73] P. Ma, Q. Luo, J. Chen, Y. Gan, J. Du, S. Ding, Z. Xi, X. Yang, Intraperitoneal injection of magnetic Fe3O4-nanoparticle induces hepatic and renal tissue injury via oxidative stress in mice, Int. J. Nanomed. 7 (2012) 4809–4818, https://doi.org/10.2147/IJN.S34349.
[74] S. Lakshmnarayanan, M.F. Shereen, K.L. Niraimathi, P. Brindha, A. Arumugam, One-pot green synthesis of iron oxide nanoparticles from Bauhinia tomentosa: characterization and application towards synthesis of 1, 3 diolein, Sci. Rep. 11 (2021), https://doi.org/10.1038/s41598-021-87960-y.
[75] H. Esmaeili, S. Tamjidi, Ultrasonic-assisted synthesis of natural clay/Fe 3 O 4/graphene oxide for enhance removal of Cr (VI) from aqueous media, Environ. Sci. Pollut. Control Ser. 27 (2020) 31652–31664, https://doi.org/10.1007/s11356-020-09448-y/Published, n.d.
[76] G. Vinodha, P.D. Shima, L. Cindrella, Mesoporous magnetite nanoparticle-decorated graphene oxide nanosheets for efficient electrochemical detection of hydrazine, J. Mater. Sci. 54 (2019) 4073–4088, https://doi.org/10.1007/s10853-018-3145-z.
[77] X. Ni, J. Zhang, L. Zhao, F. Wang, H. He, P. Dramou, Study of the solvothermal method time variation effects on magnetic iron oxide nanoparticles (Fe3O4) features, J. Phys. Chem. Solid. 169 (2022), https://doi.org/10.1016/j.jpcs.2022.110855.
[78] Y. Cheng, S. Yang, T. E, Magnetic graphene oxide prepared via ammonia coprecipitation method: the effects of preserved functional groups on adsorption property, Inorg. Chem. Commun. 128 (2021), https://doi.org/10.1016/j.inoche.2021.108603.
[79] H. Wang, G. Liu, C. Chen, W. Tu, Y. Lu, S. Wu, D. O'Hare, R. Xu, Single-Ni sites embedded in multilayer nitrogen-doped graphene derived from amino-functionalized MOF for highly selective CO2Electroreduction, ACS Sustain. Chem. Eng. 9 (2021) 3792–3801, https://doi.org/10.1021/acssuschemeng.0c08749.
[80] M.U. Kahveci, G. Acik, Y. Yagci, Synthesis of block copolymers by combination of atom transfer radical polymerization and visible light-induced free radical promoted cationic polymerization, Macromol. Rapid Commun. 33 (2012) 309–313, https://doi.org/10.1002/marc.201100641.
[81] A. Wang, M. Qiao, J. Xu, Y. Pan, Q. Ran, S. Wu, Q. Chen, POEGMA-b-PAA comb-like polymer dispersant for Al2 suspensions, J. Appl. Polym. Sci. 133 (2016), https://doi.org/10.1002/app.43352.
[82] M.M. Vantangoli, S.J. Madnick, S.M. Huse, P. Weston, K. Boekelheide, MCF-7 human breast cancer cells form differentiated microtissues in scaffold-free hydrogels, PLoS One 10 (2015), https://doi.org/10.1371/journal.pone.0135426.
[83] Q. Feng, Y. Liu, J. Huang, K. Chen, J. Huang, K. Xiao, Uptake, distribution, clearance, and toxicity of iron oxide nanoparticles with different sizes and coatings, Sci. Rep. 8 (2018), https://doi.org/10.1038/s41598-018-19628-z.
[84] H. Wei, Y. Hu, J. Wang, X. Gao, X. Qian, M. Tang, Superparamagnetic iron oxide nanoparticles: cytotoxicity, metabolism, and cellular behavior in biomedicine applications, Int. J. Nanomed. 16 (2021) 6097–6113, https://doi.org/10.2147/IJN.S321984.
[85] A.K. Tangra, G. Singh, Investigation of cytotoxicity of superparamagnetic KFeO2 nanoparticles on MCF-7 cell lines for biomedical applications, J. Mater. Sci. Mater. Electron. 32 (2021) 11232–11242, https://doi.org/10.1007/s10854-021-05793-x.
[86] J. Markhulia, S. Kekutia, V. Mikelashvili, L. Saneblidze, T. Tsertsvadze, N. Maisuradze, N. Leladze, Z. Czigány, L. Almásy, Synthesis, characterization, and in vitro cytotoxicity evaluation of doxorubicin-loaded magnetite nanoparticles on triple-negative breast cancer cell lines, Pharmaceutics 15 (2023), https://doi.org/10.3390/pharmaceutics15061758.